

BAND STRUCTURE AND ELECTRONIC PROPERTIES OF EDGE
FUNCTIONALIZED GERMANENE NANORIBBONS

by

Alexander B. Goldstone

A Thesis

Submitted to the

Graduate Faculty

of

George Mason University

In Partial Fulfillment of

The Requirements for the Degree

of

Master of Science

Electrical Engineering

Committee:

_____	Dr. Qiliang Li, Thesis Director
_____	Dr. Rao Mulpuri, Committee Member
_____	Dr. Alok Berry, Committee Member
_____	Dr. Monson Hayes, Chairman, Department of Electrical and Computer Engineering
_____	Dr. Kenneth S. Ball, Dean, College of Engineering and Computing
Date: _____	Fall Semester 2021 George Mason University Fairfax, VA

Band Structure and Electronic Properties of Edge Functionalized Germanene Nanoribbons

A thesis submitted in partial fulfillment of the requirements for the degree of
Master of Science at George Mason University

By

Alexander B. Goldstone
Bachelor of Science
George Mason University, 2016

Director: Dr. Qiliang Li, Professor
Department of Electrical and Computer Engineering

Fall Semester 2021
George Mason University
Fairfax, VA

Copyright © 2021 by Alexander B. Goldstone
All Rights Reserved

Dedication

This thesis is dedicated to my grandma, Rita Saleman, for her endless love throughout my life and enthusiasm for my pursuit of higher education.

Acknowledgments

I would like to thank my professors, Dr. Li and Dr. Mulpuri, for providing me this research opportunity. And above all my parents; without their love and support I would not be here today.

Table of Contents

	Page
List of Tables	vi
List of Figures	vii
Abstract	ix
1 Introduction	1
1.1 Graphene and the Advent of 2D Materials	1
1.2 Topological Semimetals	2
1.3 Germanene and other Group IV TSMs	8
1.4 Nanoribbon Fundamentals	12
1.5 Studies on Germanene Nanoribbons	14
2 Methods	18
2.1 Density Functional Theory: An Introduction	18
2.1.1 The Schrodinger Equation	18
2.1.2 Reduction of the Schrodinger Equation to the Electron Density Model	19
2.1.3 The Development of Density Functional Theory	22
2.2 Exchange-Correlation Functionals and Pseudopotentials	25
2.3 ATK: Geometry Optimization and Bandstructure Calculations	28
3 Results	30
3.1 Mono-Layer Germanene Sheet	30
3.2 Bilayer Germanene van der Waals Structure	31
3.3 Hydrogen Passivated Armchair Germanene Nanoribbon	32
3.4 Geometric Properties of Edge-Functionalized AC Ge Nanoribbons	34
3.5 Effect of Width on Band Gap of Edge-Functionalized AC Ge Nanoribbons .	37
3.6 Effect of Strain on H-Passivated Ge ACNR Band Structure	45
3.7 H-passivated Zigzag Germanene Nanoribbons	46
3.8 Edge-Functionalized ZZ Ge Nanoribbons	48
4 Discussion and Future Research	50
5 Conclusion	52
Bibliography	53

List of Tables

Table	Page
1.1 Properties of Group IV 2D TSMs	9

List of Figures

Figure	Page
1.1 Band structure of graphene	3
1.2 Chemical bonds in graphene	6
1.3 Buckling of germanene	7
1.4 Nodal line semimetal band structure	8
1.5 STM of silicene on Ag(111)	10
1.6 Synthesis of germanene	11
1.7 Nanoribbon directions: armchair and zigzag	12
1.8 Graphene zigzag nanoribbon edge states	14
1.9 Edge states in zigzag germanene nanoribbons	15
1.10 Band gap vs width relationship of germanene armchair nanoribbons	17
2.1 Flow chart for DFT calculations	25
2.2 Pseudopotential approximation	28
3.1 Germanene monolayer geometry and band structure	30
3.2 Germanene bilayer band structure	31
3.3 Germanene bilayer geometry	32
3.4 H-passivated Ge armchair nanoribbon	33
3.5 H-passivated Ge ACNR band structures	34
3.6 Bonding of edge species on Ge ACNRs	35
3.7 Placement of edge species within the Ge lattice	36
3.8 Bond inversion in Ge ACNRs	36
3.9 C edge-functionalized Ge ACNR band gap vs width	37
3.10 P edge-functionalized Ge ACNR band gap vs width	38
3.11 As edge-functionalized Ge ACNR band gap vs width	39
3.12 S edge-functionalized Ge ACNR band gap vs width	40
3.13 Se edge-functionalized Ge ACNR band gap vs width	40
3.14 Te edge-functionalized Ge ACNR band gap vs width	41
3.15 Band structure of F-passivated Ge ACNRs vs Monshi et. al. results	43
3.16 Halogen edge-functionalized Ge ACNRs	44

3.17	Effect of strain on H-passivated Ge ACNR band gaps	46
3.18	Geometry of H-passivated Ge ZZNRs	47
3.19	Band structures of H-passivated Ge ZZNRs	47
3.20	Geometry of edge-functionalized Ge ZZNRs	48
3.21	Band structures of edge-functionalized Ge ZZNRs	49
4.1	Comparison of band gap vs width between all Ge ACNRs	51

Abstract

BAND STRUCTURE AND ELECTRONIC PROPERTIES OF EDGE FUNCTIONALIZED GERMANENE NANORIBBONS

Alexander B. Goldstone

George Mason University, 2021

Thesis Director: Dr. Qiliang Li

In the wake of the discovery of graphene, the search for new and remarkable 2D materials with astounding electronic and mechanical properties has led to the fabrication of germanene, a 2D germanium allotrope similar to silicene. Unlike the planar structure of the graphene lattice, germanene has a buckled honeycomb structure with two vertically displaced sublattices. Free-standing germanene is a semimetal where the electrons behave as massless relativistic particles leading to enhanced carrier mobility. Indeed, recent studies have shown germanene to have an intrinsic carrier mobility on the order of $6 \times 10^5 \text{ cm}^2 \text{V}^{-1} \text{s}^{-1}$, more than double that of graphene's. Another advantage over graphene is germanene's larger spin-orbit gap (23 meV), which when compared to graphene's ($< 0.05 \text{ meV}$) makes germanene a superior candidate to exhibit the quantum spin Hall effect at experimentally viable temperatures. Lastly, the germanene lattice allows for an opening of the band gap via an applied electric field or adsorption of foreign atoms, enabling the creation of germanene based field-effect devices. In this thesis we analyze the effect of edge-functionalizing species H, C, N, P, As, O, S, Se, Te, F, Cl, Br, and I on the electronic and geometric properties of germanene armchair and zigzag nanoribbons. The effect of strain application on the band gap of H-passivated armchair nanoribbons is also examined.

We found that for each species, the armchair nanoribbons transition between semiconductor and semimetal in a cyclical pattern depending on width. The band gap of the nanoribbon, as well as the semimetal point, are tunable through width, edge-functionalization, and mechanical strain. In the case of zigzag germanene nanoribbons, the ribbons are nodal semimetals at small atomic widths but transition to metallic behavior at higher widths. While the metallic nature of large zigzag nanoribbons has been studied, the nodal semimetal behavior of thin (4-8 atoms wide) zigzag germanene ribbons is previously unreported. The different edge species reveal distinct groups showing similarities in both the geometric structure and band structure of the zigzag nanoribbons over various widths. The tunability of the band gap in germanene armchair nanoribbons nearly covers the entire infrared spectrum, a property only previously realized in HgCdTe.

Chapter 1: Introduction

1.1 Graphene and the Advent of 2D Materials

2D Materials are a major subject of interest in the emerging field of nanotechnology. The potential applications are far reaching, including industries such as health and medicine, electronics, transportation, and renewable energy [1]. National initiatives for advances in graphene and other 2D materials are being undertaken by the world's leading powers, such as the EU's Graphene Flagship program and the United States' National Nanotechnology Initiative [2][3]. In recent years the field has seen significant research investment from China, Japan, and India [4]. The concept of 2D materials, an atomically thin free-standing monolayer, has been understood for over a century. In the 1930s physicists Landau and Peierls asserted that strictly two-dimensional crystals could not exist due to being thermodynamically unstable [5][6]. While this view persisted until the recent isolation of graphene, fundamental theoretical research on the properties of such a monolayer continued. In 1947 P.R. Wallace published his Band Theory of Graphite. To better understand the electronic properties, Wallace developed a model for a two-dimensional monolayer of graphite and analyzed the limits of its properties as more layers were stacked until bulk graphite was achieved. Wallace himself, however, did not believe this 2D monolayer could be physically isolated [7]. Building on this research, Gordon Walter Semenoff, David P. DiVincenzo and Eugene J. Mele noted the emergent massless Dirac equation as the governing principle of carriers in the theoretical graphite monolayer, as opposed to Schrodinger's equation in the bulk. This work, first published in 1984, accurately predicted both the semimetal properties of graphene and the existence of an electronic Landau level at the Dirac point, resulting in the anomalous integer quantum Hall effect [8]. A consensus was emerging in the scientific community that monolayer materials had unique electronic and physical properties

not found in their bulk counterparts, resulting from the dominance of quantum effects at the nanoscopic level. Finally, in 2004 Andre Geim and Konstantin Novoselov succeeded in isolating a single layer of graphene utilizing what is now known as the 'scotch tape method'. For this discovery they jointly shared the 2010 Nobel Prize in physics [9]. Shortly after a race for the fabrication of new 2D materials began, resulting in the fabrication of numerous materials with properties surpassing even those of graphene. Today, 2D materials fall into multiple classes, from elemental semimetals such as silicene and germanene to 2D transition metal dichalcogenides (TMDCs) like MoS₂ and WS₂. Through this work a new class of 3D materials known as topological insulators was discovered which have semimetal properties at the surface.

1.2 Topological Semimetals

A *semimetal* is a 2D material with zero band gap, while a *topological insulator*, or *TI*, is a 3D material with zero band gap surface states and a non-zero band gap in the bulk. There exist materials between planar semimetals and topological insulators known as *topological semimetals* or *TSMs* [10]. Unlike graphene these materials are non-planar but nonetheless lack a band gap in the bulk [11]. The zero band gap states in TSMs result from a linear dispersion of the valence and conduction bands which touch at a single point. This point is known as the Dirac point and the linear band dispersion is called a Dirac cone. The presence of Dirac cones in the band structure is a standard property of TSMs.

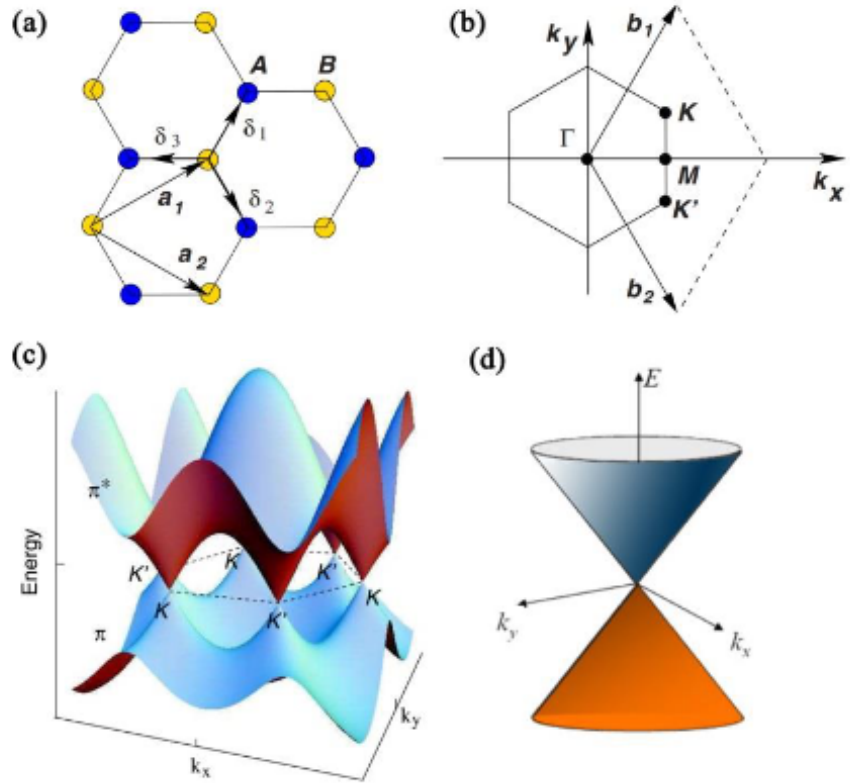


Figure 1.1: (a) The lattice vectors of graphene, (b) the graphene unit cell in reciprocal space, (c) band structure of graphene, (d) the Dirac cone [12]

The emergence of the Dirac cone can be understood both mathematically and physically. Graphene forms a planar hexagonal structure of carbon atoms with each sharing three C-C covalent bonds of length $a = 1.42\text{\AA}$. The unit cell is a triangular lattice consisting of two carbon atoms with lattice vectors:

$$a_1 = \frac{a}{2}(3, \sqrt{3}) \quad a_2 = \frac{a}{2}(3, -\sqrt{3})$$

In reciprocal space these vectors take the form

$$b_1 = \frac{2\pi}{3a}(1, \sqrt{3}) \quad b_2 = \frac{2\pi}{3a}(1, -\sqrt{3})$$

The two points in the Brillouin zone where the Dirac cones form are K and K' whose positions in momentum space are

$$K = \left(\frac{2\pi}{3a}, \frac{2\pi}{3\sqrt{3}a}\right) \quad K' = \left(\frac{2\pi}{3a}, -\frac{2\pi}{3\sqrt{3}a}\right)$$

P.R. Wallace was the first to derive the electronic structure from the tight-binding model by utilizing the nearest-neighbor hopping Hamiltonian

$$\hat{H} = -\gamma_0 \sum_{\langle ij \rangle} (\hat{a}_i^\dagger \hat{b}_j + \hat{b}_j^\dagger \hat{a}_i)$$

where $\gamma_0 = 3.15$ eV is the nearest-neighbor hopping energy, i and j denote sites on sublattices A and B respectively, the operator \hat{a}_i^\dagger creates an electron at position r_i of sublattice A , and \hat{a}_i annihilates an electron. The b operators behave similarly but represent the nearest neighboring atom. From [7], Wallace derived the energy levels as

$$E(\vec{k}) = \pm \sqrt{1 + 4 \cos\left(\frac{3}{2}k_x a\right) \cos\left(\frac{\sqrt{3}}{2}k_y a\right) + 4 \cos^2\left(\frac{\sqrt{3}}{2}k_y a\right)}$$

As we approach the K and K' points the momentum vector becomes $\vec{k} = \vec{K} + \delta k$ and the energy levels reduce to

$$E_{\pm}(\vec{k}) = \pm \hbar v_f |\vec{\delta k}|$$

where $|\vec{\delta k}| \ll |\vec{K}|$ and the Fermi velocity v_f is

$$v_f = \frac{3a\gamma_0}{2\hbar}$$

This result shows a linear relationship for both energy and Fermi velocity. Remarkably, the Fermi velocity derived here is independent of energy or momentum, as in the more traditional case $v = \sqrt{2E/m}$ [13]. This result shows the electrons in graphene behave as massless relativistic particles, and are described by the Dirac equation as opposed to Schrodinger's equation. For more details on this derivation see [13] [14] [15] [16]. It is this relativistic behavior near the Dirac points that leads to the high carrier mobilities not seen in traditional semiconductors. Indeed, graphene has been experimentally shown to have carrier mobilities on the order of $1 \times 10^5 \text{ cm}^2 \text{V}^{-1} \text{s}^{-1}$. The emergence of this carrier behavior can also be understood chemically from the arrangement of bonds in the graphene structure.

Chemically, graphene is a hexagonal lattice of carbon atoms bound together by sp^2 hybridized σ -bonds. Since carbon has four valence electrons, three are used to form σ -bonds while the remaining electron occupies the p_z orbital. Importantly, all the C-C bonds in graphene are of the same length which delocalizes the remaining electrons across the entire graphene sheet. These electron orbitals then form strong π -bonds spread evenly throughout the system. The tight-binding model as derived by Wallace shows that the bonding and anti-bonding components of the p_z band are degenerate about the K (and thus K') point. This two-fold degeneracy is responsible for the formation of the Dirac cone, but alone does not explain the system's stability.

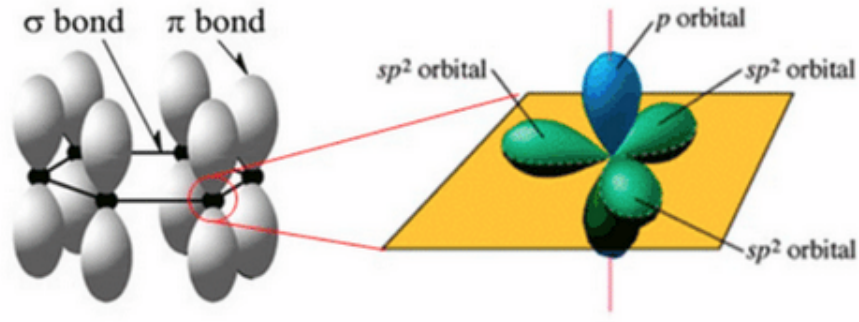


Figure 1.2: Visualization of the σ and π bonds in the graphene lattice [17]

Typically, we would expect a Peierls distortion, that is a formation of stronger bonds between neighboring atoms to separate the degenerate states. That in turn should pull neighboring atoms closer together, but the strong delocalized π -bonds energetically stabilize the system and prevent the C-C bond lengths from changing. This ensures the Dirac cone is 'symmetry protected' [11]. This, however, does not prevent other methods from opening a band gap in the material; a requirement for use in field-effect based devices [16][18]. This opening can be created using a multitude of methods: doping of the graphene sheet, adjusting bond length through application of strain, applying an external electric field, and applying relativistic effects via spin-orbit coupling. While the spin-orbit gap in graphene is extremely small (< 0.05 meV), this gap is larger in heavier monolayer graphene analogues and more complex topological insulators. The transition from a planar semimetal to a 3D topological insulator can be easily understood from analyzing the stability of graphene's closest cousins: the group IV monolayer materials silicene, germanene, and stanene. π -bonds become less stable as atomic mass increases, and in carbon's heavier cousins the atoms will want to form a fourth σ -bond and buckle into 3D silicon, germanium and tin. However, after a certain buckling height Δ , the atoms become close enough that the p_z -orbitals form a stable delocalized π -system. The heavier the atom, the larger the buckling height.

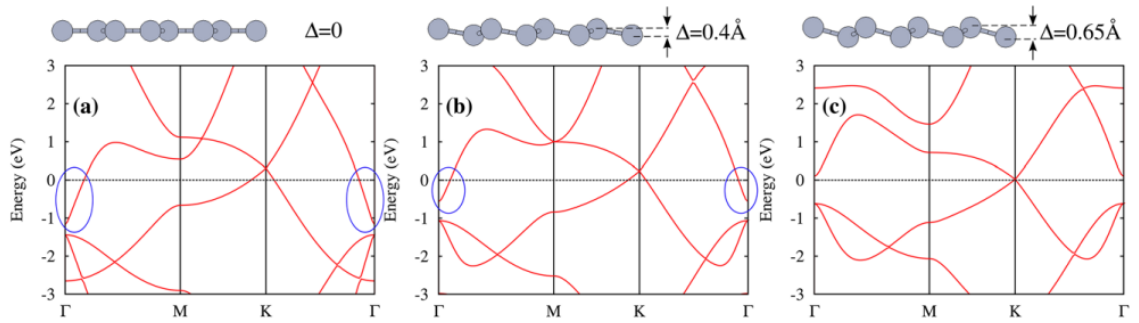


Figure 1.3: Buckling in a germanene sheet. The planar form (a) is unstable. To align the Dirac point with the Fermi level the material buckles to a distance of $\Delta = 0.65\text{\AA}$ (c) [18].

There are many different classes of both TSMs and TIs, each with different elements and physics governing their topological properties. A detailed reference for these diverse topological classes can be found here [11] [19]. The last class relevant to our discussion on germanene are the *nodal line semimetals*. In a nodal line semimetal, the degenerate states exist not just at a point, but have lines as Fermi surfaces. In these materials the concentration of Dirac electrons is much greater than in standard semimetals, and have potential use as superconductors and magnetic sensors [11]. As we will see later in this thesis, zigzag germanene nanoribbons form nodal line semimetals at low atomic widths.

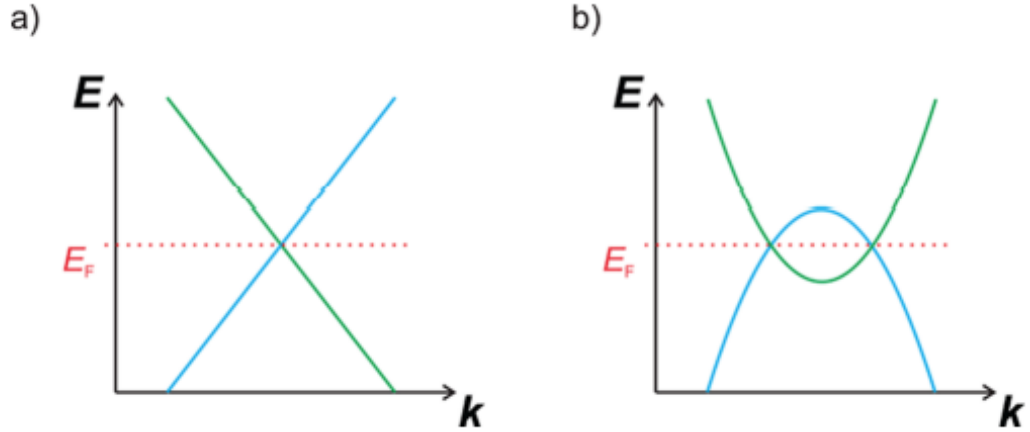


Figure 1.4: (a) Semimetal band structure with single Dirac point, (b) nodal line semimetal with 'looped' Fermi surface [11]

1.3 Germanene and other Group IV TSMs

In the periodic table the carbon group consists of the elements carbon, silicon, germanium, tin and lead. Following the fabrication of graphene in 2004 a stable atomic monolayer of each element has been synthesized, starting with silicene in 2012 [20] [21] and most recently plumbene in 2019 [22]. Despite all being semimetals the materials vary in both carrier mobility and spin-orbit gap. Germanene is the most promising of the materials for electronics as it has both the highest carrier mobility ($6 \times 10^5 \text{ cm}^2 \text{V}^{-1} \text{s}^{-1}$) and a sufficiently large spin-orbit gap (23 meV) to exhibit the quantum spin Hall effect at room temperature [23] [24]. Table 1.1 shows numerical values for the properties of graphene, silicene, germanene, and stanene as found in [24], [23], [24], and [25] respectively.

Attempts to create free-standing monolayers of graphene analogues has thus far proved unsuccessful, and their synthesis has only been achieved by growth on metal substrates (known as xenes) or via complex chemical stabilization methods (known as xanes). In both cases this results in a 2D TI instead of a semimetal. In the case of xenes this is due to

Table 1.1: Properties of Group IV 2D TSMs

	Graphene	Silicene	Germanene	Stanene
Bond Length (Å)	1.42	2.25	2.45	2.75
Buckling Height (Å)	0	0.44	0.67	0.85
Carrier Mobility ($\text{cm}^2\text{V}^{-1}\text{s}^{-1}$)	2×10^5	2.57×10^5	6×10^5	2.5×10^3
Spin-orbit Gap (meV)	0.005	1.55	23	73

bonding between the 2D material and the metal substrate. In the case of xanes the non-trivial topology originates from inverted σ -bonds as opposed to delocalized π -bonds making the materials more similar to HgTe than graphene. Silicene was first synthesized in 2012 by Vogt. et. al. via molecular-beam epitaxy (MBE) onto an Ag(111) substrate [20]. The resulting structure was analyzed by STM and showed a well-ordered, buckled honeycomb shape. While Si growth on Ag(111) is still the most popular method of silicene fabrication, the material has since been grown on Ir(111), ZrC(111), Al(111), as well as BN and SiC substrates [26] [27]. In each case the bonding between Si and the substrate leads to an opening of the Dirac cone with BN and SiC substrates having a larger gap than metal substrates.

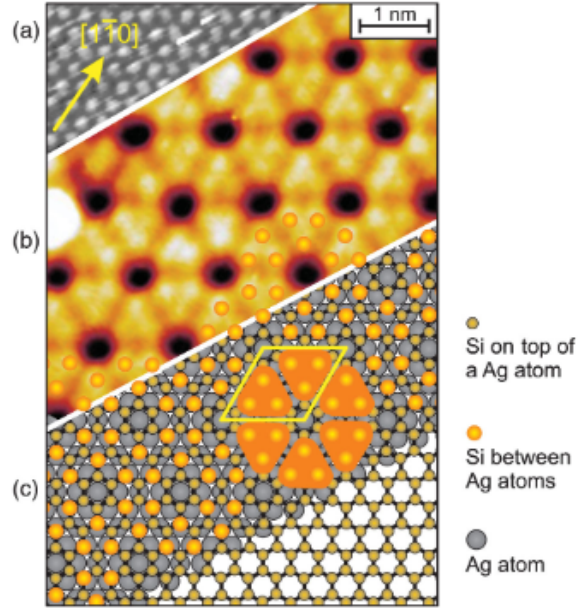


Figure 1.5: Silicene on Ag(111) [26] (a) shows the initial Ag(111) surface, (b) shows STM of the (4x4) silicene sheet, and (c) shows the simulated model for comparison

The first reported growth of germanene was carried out by Li et. al. in 2014 on a Pt(111) substrate [28]. However, their result was misinterpreted based on comparisons to the previously mentioned silicene study. The resulting Ge structures showed a disorganized Ge lattice with lopsided honeycombs on top of the Pt, but an extra layer of protruding Ge atoms formed a well-ordered 18 atom ($\sqrt{19} \times \sqrt{19}$) unit cell. It was later suggested that this was not germanene but a surface alloy of Ge_3Pt tetramers. Davila et. al. published the next attempt at germanene synthesis in 2014 [29]. Also using MBE growth, they used Au(111) for the base substrate and obtained a three phase structure consisting of a ($\sqrt{19} \times \sqrt{19}$) phase, a (5 x 5) phase, and a ($\sqrt{7} \times \sqrt{7}$) phase. The ($\sqrt{7} \times \sqrt{7}$) phase exhibited a nearly flat, highly symmetric honeycomb structure which the authors ascribed as germanene. The first single phase germanene construction was obtained by Derivaz et. al. in 2015 by growth on an Al(111) substrate [30]. This structure had a simple (3 x 3) phase that formed a

continuous layer across the aluminum with observed buckling.

Finally, Davila et. al. revisited their work the following year and achieved a single phase $(3\sqrt{3} \times 3\sqrt{3})$ Ge honeycomb structure on Au(111). For the first time, Davila et. al. were able to find experimental evidence of Dirac cones in this material and a standard method for germanene growth was achieved [31]. While an opening of the Dirac cone is desirable for applications in modern electronics, the opening created by substrate bonding is fixed and challenging to manipulate. If free-standing germanene can be achieved a more ideal method for opening and tuning of the band gap would be the creation of germanene nanoribbons, where the band gap results from the effects of quantum confinement.

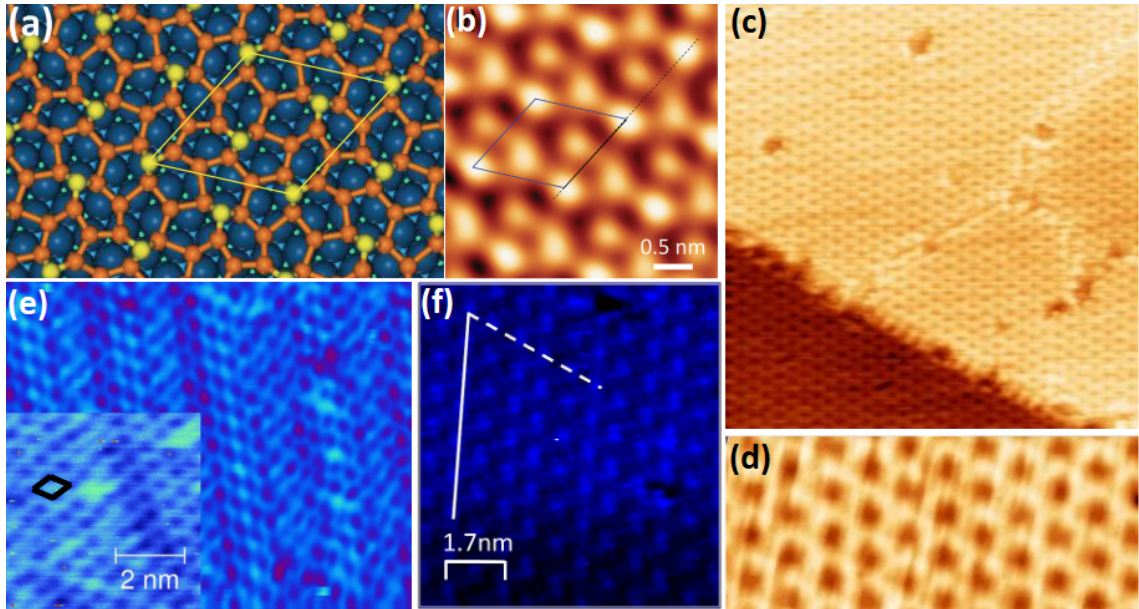


Figure 1.6: The synthesis of germanene: Ge₃Pt growth on Pt(111) (a-b) [28], Ge on Al(111) (c-d) [30], three phase germanene on Au(111) (e) [29], and single phase germanene on Au(111) [31]

1.4 Nanoribbon Fundamentals

The opening of graphene's band gap is paramount to its use in digital electronic devices, which depend on precise control of the band gap for on/off switching. One popular method is to exploit electronic confinement as utilized in quantum wells and quantum dots. An elegant solution to this is the creation of graphene nanoribbons, a one dimensional material with theoretically infinite length but a fixed width. Since graphene is hexagonal in structure, nanoribbons are created by cutting along the $[10\bar{1}0]$ and $[11\bar{2}0]$ directions which form armchair (AC) and zigzag (ZZ) nanoribbons respectively [32]. The termination of the graphene lattice leaves dangling bonds which give rise to electronic edge states. To differentiate these edge atoms from the bulk they are modeled with a negative on-site energy $\epsilon_{edge} < 0$ eV while the bulk atoms are modeled by $\epsilon_{bulk} = 0$ eV. This application of negative energy mimics the effect of passivating the dangling bonds with hydrogen. Indeed, the difference between the electron affinities of carbon and hydrogen atoms is in fact ϵ_{edge} [33].

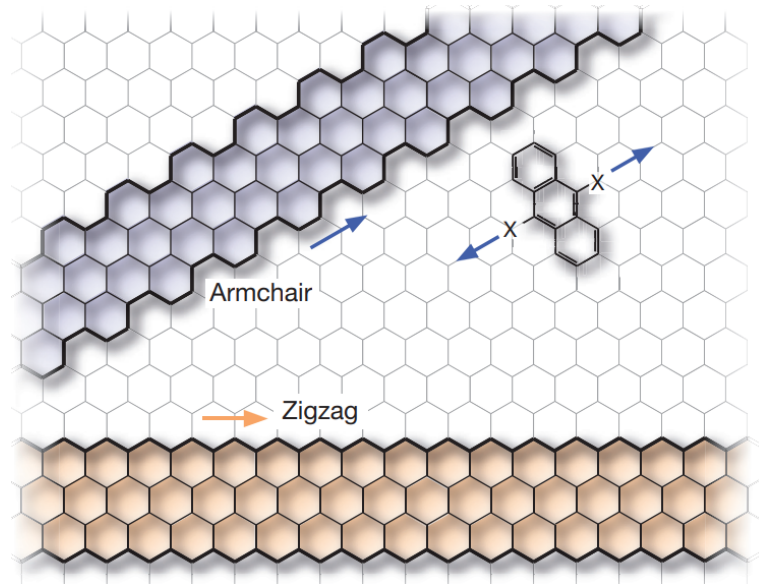


Figure 1.7: Armchair and zigzag direction on a graphene sheet [34]

The direction of the nanoribbons have significant impact on their electronic properties which arises from their differing boundary conditions. The atoms along the edge of ZZNRs come from the same sublattice while atoms along the ACNR edge come from different sublattices. AC graphene nanoribbons are metallic or semiconducting with an inversally proportional band gap to width relationship [32][33]. The width is defined by the integer value 'm', which classifies AC nanoribbons into three categories: $m = 3p$, $m = 3p + 1$ and $m = 3p + 2$ where p is a positive integer. The $m = 3p + 2$ graphene nanoribbons show metallic behavior (as we will soon see, the $3p + 2$ class of germanene AC nanoribbons show semimetallic behavior) while the other classes are semiconductors. This band gap can be further adjusted by passivating the edge states with hydrogen or adsorption of foreign atoms. While ZZ graphene nanoribbons are metallic in nature, their edges contain localized electronic states where the valence and conduction bands touch at the Fermi level but do not form a Dirac cone. These states are degenerate and dispersionless up to the boundary of the Brillouin zone and result in a high density of states at the Fermi level [33][35]. This pile up of states along the edge leads to an instability that can be resolved by aligning the spin states of one edge and generating an antiparallel alignment along the other. This can be achieved by either spin polarization techniques or tuning the electronic correlations between the edges [32][33][35]. This antiparallel spin ordering leads the ground states of the edge atoms to become antiferromagnetic. This in turn opens a direct band gap at the edge which is inversly proportional to the nanoribbon's width. In contrast, by polarizing the edge states to have parallel spin the nanoribbon becomes ferromagnetic and the band gap will close resulting in metallic properties. In each case the edge states exhibit a significantly higher spin moment that decays towards the nanoribbon's center. Thus ZZ graphene nanoribbons can be used in the design of magnetic nanostructures with tunable magnetic, electronic, and spin properites [36][37][38].

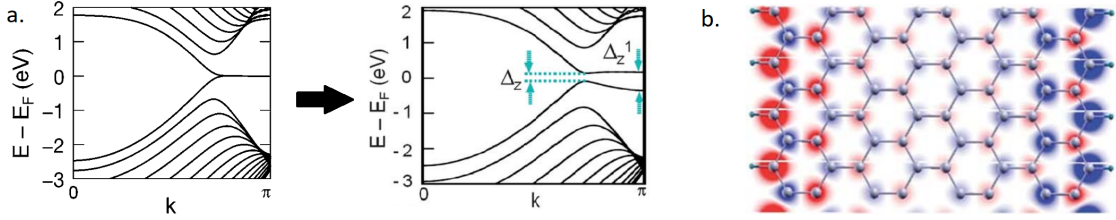


Figure 1.8: (a) Opening of the band gap in a graphene ZZNR's edge states, (b) anti-parallel alignment of spin states along the ZZNR edge. The density of states is greater along the edges and decays towards the center of the ribbon [33].

1.5 Studies on Germanene Nanoribbons

In the same year germanene was successfully synthesized, studies on the properties of germanene nanoribbons were carried out via density functional theory calculations. In 2014, Lars Matthes and Friedhelm Bechstedt carried out a study on ZZ germanene nanoribbons using the Perdew, Burke, and Ernzerhof (PBE) exchange-correlation and the general gradient approximation (GGA) [39]. They first simulated an infinite germanene sheet and noted a buckling height of $\Delta = 0.69\text{\AA}$ and the presence of a Dirac cone at the K point (the value of Δ has ranged from $0.65\text{-}0.70\text{\AA}$ among different germanene studies). When considering spin-orbit interaction (SOI) they measured the spin-orbit gap to be 24 meV, significantly larger than that of graphene and silicene. Their analysis on nanoribbons was restricted to a hydrogen edge-passivated ZZNR, particularly for a width of 16 atoms to prevent interactions between the two edges. In the non-magnetic case they noted the existence of two-fold degenerate edge states at the X point of the Brillouin zone, whereas in the case of graphene the edge states exist between the K and Z points. By applying spin polarization in either antiparallel or parallel configurations, they obtained an antiferromagnetic ribbon with an opening of the band gap about the X point and a ferromagnetic ribbon with metallic properties, similar to the graphene case. These results were later confirmed by Sharma et. al. in 2016 [40].

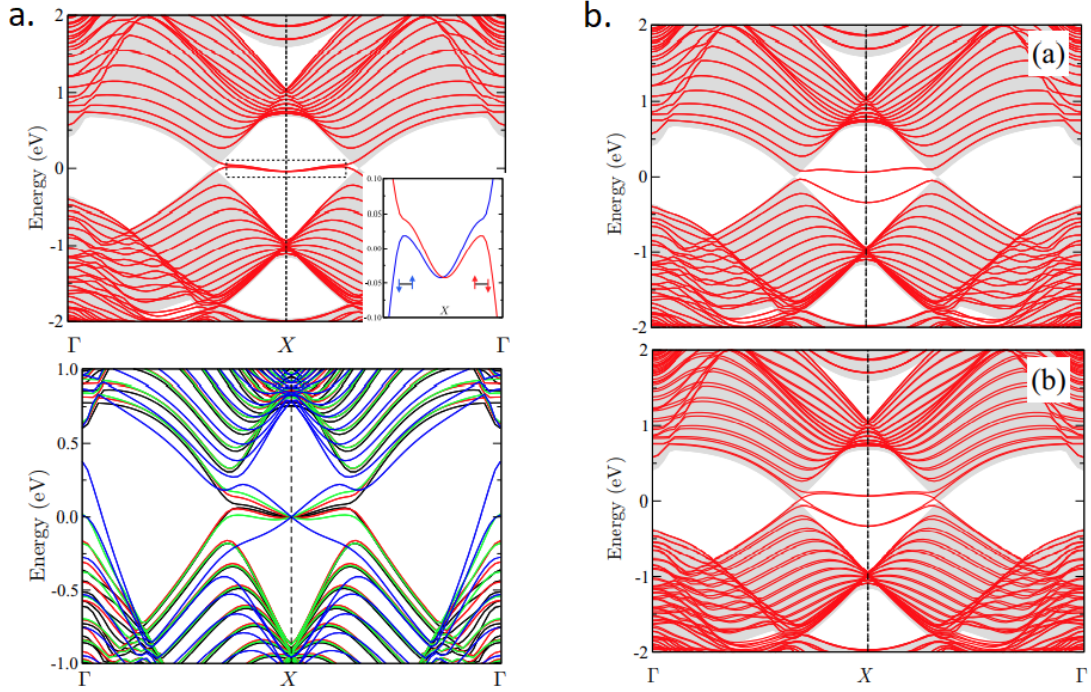


Figure 1.9: (a) Band structure of edge states in ZZ germanene nanoribbon (top) and with the effect of SOI (bottom, blue lines), (b) antiferromagnetic ribbon with opening of band gap (top) and ferromagnetic ribbon with metallic behavior (bottom) [40]

In 2017 Monshi et. al. performed a comprehensive study on mono vs di-hydrogen passivation of germanene ACNRs as well as using flourine and chlorine as edge atoms [41]. The hydrogen passivated nanoribbons showed a cyclical pattern with respect to width, showing semiconductor properties in the $3P$ and $3P+1$ classes while having semimetallic properties in the $3P+2$ class, differing from that of graphene ACNRs which are metallic in the $3P+2$ class. The band gap of the semiconductor-like ribbons decreased with width, maintaining the inversely proportional relationship. While fluorine passivation showed a similar cyclical pattern, all three classes had a non-trivial band gap whereas chlorine showed no recognizable pattern in the band gap with respect to width. Finally, in 2019 Shiraz et. al. did a comprehensive analysis of width vs band gap for the single hydrogen passivated Ge ACNR, as well as analyzing the effect of strain and its dielectric constant [42]. The same

3-atom width cyclical relationship as described by Monshi et. al. was obtained, this time explicitly noting a logarithmic decrease in the band gap of each class as width increased. A strain of -8% to 8% was applied in the transport direction of $m = 9, 10,$ and 11 width ribbons; one of each class. For each ribbon the band gap was tunable from near-trivial to 0.5 eV demonstrating significant control over the ACNR band gaps. However, no study has expanded these results to analyze the effects of edge species beyond hydrogen, fluorine, and chlorine to the band gap vs width relationship of Ge ACNRs nor the edge states of ZZNRs. In this thesis, we analyze the band structure of the infinite germanene sheet and hydrogen passivated ACNR to compare with previous studies. We then examine the separation distance and energy to form a bilayer van der Waals structure of germanene sheets and its impact on opening of the band gap, as well as the band gap vs width relationship for AC and ZZ nanoribbons with edge species C, P, As, S, Se, Te, F, Cl, Br, and I for $m = 3$ to 12 atoms in width.

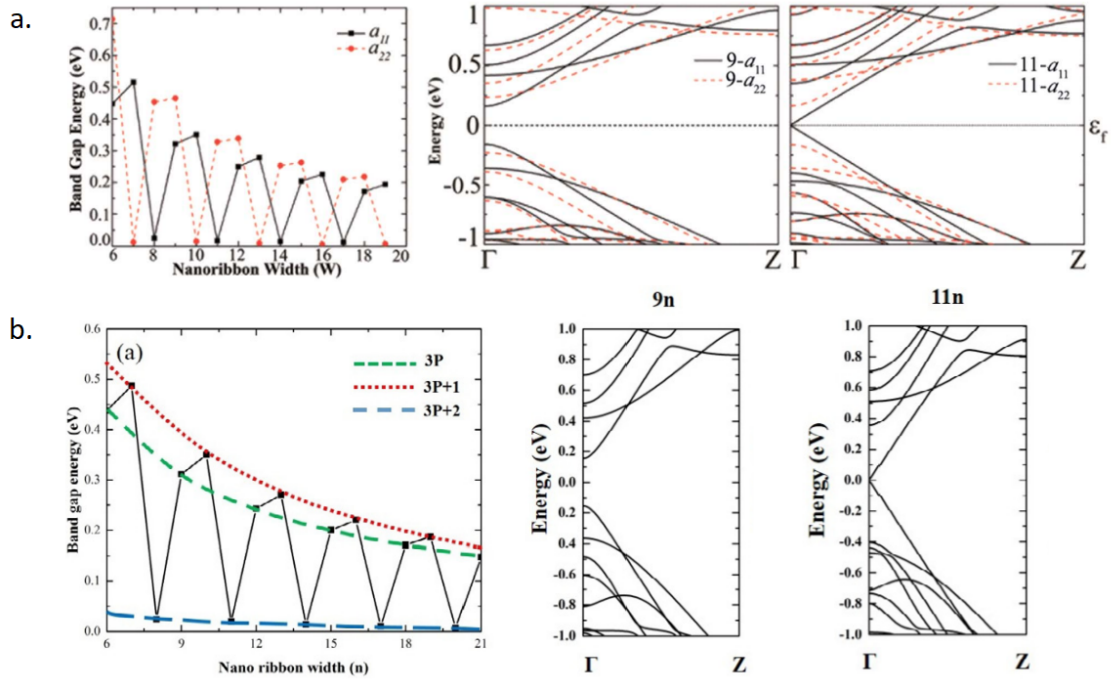


Figure 1.10: (a) Monshi et. al. results for band structure of mono and di-hydrogen passivated Ge ACNRs. The 11-atom width nanoribbon shows a linear E-K relationship and presence of a Dirac point [41] (b) Shiraz et. al. results for band gap vs width of mono-hydrogen passivated Ge ACNRs. Their graph indicates the band gap of the different width classes, with the 9-atom width showing a band gap and the 11-atom width showing a Dirac point [42].

Chapter 2: Methods

2.1 Density Functional Theory: An Introduction

Density functional theory is a computational method for modeling quantum mechanical properties and interactions. It gained popularity after physicists Walter Kohn and Lu Jeu Sham developed the Kohn-Sham equations at the University of California, San Diego in 1965. While this made DFT sufficient for solid-state physics calculations the method was too inaccurate for use in quantum chemistry. It wasn't until the 1990s that the development of advanced exchange-correlations and pseudopotentials allowed the application of DFT to quantum chemistry, after which Walter Kohn was finally awarded the Nobel Prize in chemistry for his theory in 1998 [43]. In this introduction we will briefly cover the theory with respect to calculations used in this thesis. For greater detail on this explanation, see [44].

2.1.1 The Schrodinger Equation

The Schrodinger equation is a 2nd order partial differential equation that describes the wave function of a quantum mechanical system. For a non-relativistic, time-independent system the Schrodinger equation for a many-bodied system is

$$\hat{H}\Psi(\{r_i\}, \{R_I\}) = E\Psi(\{r_i\}, \{R_I\})$$

where $\Psi(\{r_i\}, \{R_I\})$ is the wave function of the system, $\{r_i\}$ and $\{R_I\}$ are the electron and nuclear coordinates respectively, E is the energy of the system and \hat{H} is the time-independent Hamiltonian. If we let the kinetic energy of an electron or nucleus be $T_{e,n}$, the

potential energy between two nuclei be V_{n-n} , the potential energy between an electron and a nucleus be V_{e-n} , and the potential energy between two electrons be V_{e-e} where

$$T_{e,n} = -\frac{\hbar^2}{2m_{e,n}} \sum_{i,I}^{N_{e,n}} \nabla_{i,I}^2 \quad V_{n-n} = \frac{1}{2} \sum_{I \neq J}^{N_n} \frac{Z_I Z_J e^2}{|R_I - R_J|}$$

$$V_{e-n} = \left(\sum_i^{N_e} + \sum_I^{N_n} \right) \frac{Z_I e^2}{|r_i - R_I|} \quad V_{e-e} = \frac{1}{2} \sum_{i \neq j}^{N_e} \frac{e^2}{|r_i - r_j|}$$

and $m_{e,n}$ is the mass of an electron or nucleus, Z is the atomic number of the nucleus, r is the position of an electron and R is the position of a nucleus. Here, the index i sums over the number of electrons N_e and I sums over the number of nuclei N_n . With this, we can then reduce the time-independent Hamiltonian to

$$\hat{H} = T_e(\{r_i\}) + T_n(\{R_I\}) + V_{n-n}(\{R_I\}) + V_{e-n}(\{r_i\}, \{R_I\}) + V_{e-e}(\{r_i\})$$

In theory this equation should provide a complete explanation for the quantum mechanical behavior of electrons in the system, but clearly the equation is extremely expensive to solve for a many-body system. The purpose of density functional theory is to address this very issue: find a computationally inexpensive method for approximating the non-relativistic, time-independent Schrodinger equation for a many-bodied system.

2.1.2 Reduction of the Schrodinger Equation to the Electron Density Model

The first major step towards the development of DFT was taken by Born and Oppenheimer in 1927. Since nuclei are significantly heavier than electrons, they realized the timescale of an electron response must be orders of magnitude greater than that of the nuclei. Using this we can treat the electrons as evolving in the field of fixed nuclei, which yields the following

Hamiltonian:

$$\hat{H}_e = T_e(\{r_i\}) + V_{e-n}(\{r_i\}, \{R_I\}) + V_{e-e}(\{r_i\})$$

The solution to the Schrodinger equation with this Hamiltonian is

$$\hat{H}_e \Psi_e(\{r_i, \sigma_i\}, \{R_I\}) = E_e \Psi_e(\{r_i, \sigma_i\}, \{R_I\})$$

We note that for fixed nuclei, $\{R_I\}$ is a constant set of parameters and the equation is a function of only the electron coordinates $\{r_i, \sigma_i\}$. Then if we combine the electron's spatial and spin coordinates $\{r_i, \sigma_i\}$ to $\{x_i\}$ we can further reduce the equation to

$$\hat{H}_e \Psi_e(\{x_i\}) = E_e \Psi_e(\{x_i\})$$

The total energy, assuming positions of the nuclei are known, is the sum of the total electron energy E_e and the potential energy between the nuclei V_{n-n} , giving us

$$E_{tot} = E_e + V_{n-n}(\{R_I\})$$

This greatly simplifies the approximation of the many-bodied system, reducing the problem to solving the electron system. However, solving for the electron-electron interaction $V_{e-e}(\{r_i\})$ involves 3^{N_e} variables for an N_e electron system leaving the problem intractable in its current form. Hartree and Fock developed a theoretical solution to this problem in 1935 but calculations were too complex to be carried out by hand. It was not widely used until computational power evolved in the mid 1950s. The Hartree-Fock approximation was a monumental step in the development of quantum chemistry. It was through this method that applying the concept of electron density in conjunction with the variational principle was first apparent, and this combination forms the basis of density functional theory.

In 1927 D. R. Hartree developed a procedure to approximate the wave functions of atoms. He chose to approach the Schrodinger equation from fundamental physical principles, a method known as *ab initio*. Considering that each electron moves independently within its own orbital, it sees only the *average* potential generated by all other electrons. By applying this concept Hartree reduced the potential energy of the system to a sum of two potentials: the external Coulomb potential $V_{ext}(x_i)$, consisting of the electron-nuclei interactions and nucleus to nucleus interactions, and what he dubbed the Hartree potential $V_H(x_i)$. This potential is approximated by an average single electron potential expressed by the Coulomb repulsion between that electron and the *electron density* of all other electrons in the system. This results in the equation

$$\left[-\frac{\hbar}{2m} \nabla^2 + V_{ext}(x_i) + V_H(x_i) \right] \psi_i(x_i) = \epsilon_i \psi_i(x_i)$$

In this theory, where the wave function of a single electron is $\psi_i(x_i)$, the resulting wave function for the system would be the product

$$\Psi(x_i) = \prod_i^{N_e} \psi(x_i)$$

Hartree's method was met with mixed response from the scientific community. In 1928 Slater and Gaunt independently demonstrated the Hartree method would have a stronger theoretical basis by incorporating the variational principle, which states that the expected value of the electronic Hamiltonian \hat{H}_e for any trial wavefunction is always greater than or equal to the electronic ground state energy $E_0[\Psi_0]$. This allows one to start with a trial function in place of the ground state and incrementally improve the wave function within the restricted antisymmetrized space of single particle wave functions. However, while Hartree's method accounted for the Pauli exclusion principle it ignored the fermionic nature of electrons and thus violated the principle of antisymmetry. Not only did this make

his method invalid, it prevented the application of the variational principle. In 1930 Slater and Fock independently noted this discrepancy, and Fock proposed a solution by using a Slater determinant. This determinant, which is a linear combination of the product of independent electron wavefunctions that accounts for all coordinate permutations, would satisfy the antisymmetric property and allow for the application of the variational principle. This is accounted for by adding an additional term in the potential $V_X(x_i)$ which yields

$$\left[-\frac{\hbar}{2m} \nabla^2 + V_{ext}(x_i) + V_H(x_i) + V_X(x_i) \right] \psi_i(x_i) = \epsilon_i \psi_i(x_i)$$

This method is known as the Hartree-Fock method, and would be the dominant method for approximating the Schrodinger equation for multi-body systems until the development of DFT in 1964.

2.1.3 The Development of Density Functional Theory

The primary advantage of DFT is using the electron density $n(r)$ in place of individual electron wavefunctions. For an N_e electron system, regardless of size, the density is always three-dimensional. This allows DFT to be applied to systems with thousands of atoms and is only restricted by modern computing power. We can express the electron density $n(r)$ as

$$n(r) = N_e \int |\Psi(x_1, x_2, \dots, x_{N_e})|^2 d\sigma_1 d\sigma_2 \dots d\sigma_{N_e}$$

Consequently, integrating this density over the volume r in turn yields the total number of electrons, so

$$N_e = \int n(r) dr$$

Hohenberg and Kohn developed DFT in 1964 based on two founding principles: there exists a one-to-one correspondence between the external potential $v(r)$ of a system and its

electron density $n(\mathbf{r})$, and the ground state electron density can be obtained utilizing the variational principle. Since there exists a one-to-one correspondence between $v(\mathbf{r})$ and $n(\mathbf{r})$, we can define the energy of the system as

$$E_v[n(\mathbf{r})] = T[n(\mathbf{r})] + V_{n-e}[n(\mathbf{r})] + V_{e-e}[n(\mathbf{r})]$$

The potential energy term for interactions between the electrons and nuclei of the system $V_{n-e}[n(\mathbf{r})]$ can be described by integrating the product of the electron density and the external potential of the system which yields

$$E_v[n(\mathbf{r})] = \int n(\mathbf{r})v(\mathbf{r})d\mathbf{r} + F_{HK}[n(\mathbf{r})]$$

where $F_{HK}[n(\mathbf{r})] = T[n(\mathbf{r})] + V_{e-e}[n(\mathbf{r})]$. We then apply the variational principle, which in this case states that $E_0[n_0(\mathbf{r})] \leq E_v[n(\mathbf{r})]$. This implies that

$$E_v[n(\mathbf{r})] = \int n(\mathbf{r})v(\mathbf{r})d\mathbf{r} + F_{HK}[n(\mathbf{r})] \geq E_0$$

Now the problem is reduced to minimizing the F_{HK} term. Previous attempts at applying similar methods, as with the Thomas-Fermi theory, failed to adequately describe the kinetic energy. To address this Kohn and Sham expanded the F_{HK} term to a sum of the kinetic energy of noninteracting electrons T_S , the Hartree energy E_H , and combined the remaining many-body quantum effects into the exchange and correlation energy E_{xc} . By minimizing $F_{HK}[n(\mathbf{r})]$ under the constraint of orthonormality for one-particle orbitals ψ_i they derived a set of N_e single particle equations known as the Kohn-Sham equations, which take the form

$$\left[-\frac{\hbar^2}{2m_e} \nabla^2 + \nu_{KS}[n(\mathbf{r})] \right] \psi_i(\mathbf{r}) = \hat{H}_{KS}\psi_i(\mathbf{r}) = \epsilon_i\psi_r$$

where the electron density $n(\mathbf{r})$ can be written as

$$n(\mathbf{r}) = \sum_{i=1}^{N_e} |\psi_i|^2$$

and the effective potential experienced by the electrons, $\nu_{KS}[n(\mathbf{r})]$, is

$$\begin{aligned} \nu_{KS}[n(\mathbf{r})] &= \frac{\delta}{\delta n(\mathbf{r})} \int n(\mathbf{r})v(\mathbf{r})d\mathbf{r} + T_S[n(\mathbf{r})] + E_H[n(\mathbf{r})] + E_{xc}[n(\mathbf{r})] \\ &= v[n(\mathbf{r})] + \int \frac{n(\mathbf{r}')}{|\mathbf{r} - \mathbf{r}'|}d\mathbf{r}' + \nu_{xc}[n(\mathbf{r})] \end{aligned}$$

The exchange correlation potential ν_{xc} is then defined as

$$\nu_{xc}[n(\mathbf{r})] = \frac{\delta E_{xc}[n(\mathbf{r})]}{\delta n(\mathbf{r})}$$

With this, we can calculate the total energy of the system with the following equation

$$E = \sum_{i=1}^{N_e} \epsilon_i - \frac{1}{2} \iint \frac{n(\mathbf{r})n(\mathbf{r}')}{|\mathbf{r} - \mathbf{r}'|} + E_{xc}[n] - \int \nu_{xc}[n(\mathbf{r})]n(\mathbf{r})d\mathbf{r}$$

We now have the tools to understand the general procedure for DFT calculations. The Kohn-Sham equations are solved self-consistently, meaning the solution satisfies each of the N_e equations. We start with an initial guess for the electron density $n_0(\mathbf{r})$ and construct the corresponding $v(\mathbf{r})$ from the equation for $E[n(\mathbf{r})]$. We then solve the Kohn-Sham equations for the orbitals $\psi_i(\mathbf{r})$ and use them to construct a new electron density $n(\mathbf{r})$. We then repeat the process with the new electron density until they converge (Figure 2.1). The problem with this method is the exchange-correlation E_{xc} is unknown. Multiple successful models for the exchange-correlation have been developed, most notably the local density

approximation (LDA) and general gradient approximation (GGA), the latter of which is used throughout this thesis.

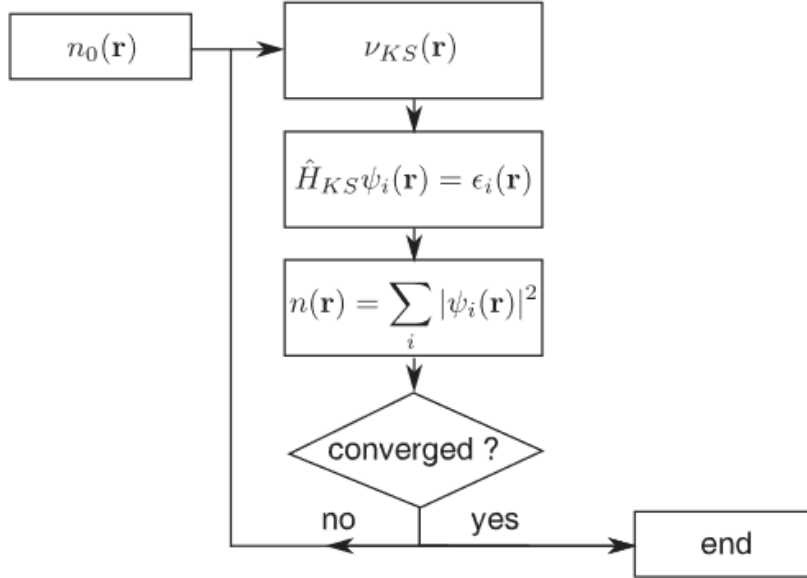


Figure 2.1: Flow chart for self-consistent DFT calculations [44]

2.2 Exchange-Correlation Functionals and Pseudopotentials

The first exchange-correlation proposed by Kohn and Sham is the local density approximation (LDA). In this method, the inhomogeneous system is divided into infinitesimal volumes of constant electron density. We then approximate the correlation energy per electron at point \mathbf{r} , $\epsilon_{xc}[n(\mathbf{r})]$, by assuming it is equal to the exchange-correlation energy per electron in a homogenous electron gas with the same density as that at point \mathbf{r} . This leads to a total exchange-correlation of

$$E_{xc}^{LDA}[n(r)] = \int \epsilon_{xc}^{hom}[n(r)]n(r)dr$$

A flaw with this method is that it does not directly calculate the correlation term. Instead, it calculates the exchange term for each point r using the Dirac exchange-energy functional

$$E_x^{LDA}[n(r)] = -\frac{3}{4} \left(\frac{3n(r)}{\pi} \right)^{1/3}$$

and determines the correlation term by interpolating homogeneous electron gas data obtained from Monte-Carlo simulations. This makes the LDA most appropriate for systems where the electron density varies slowly. This method can be improved by taking into account the density gradient ($\nabla n(r)$) at points throughout the system. This leads to the general gradient approximation (GGA), which is described by the equation

$$E_{xc}^{GGA}[n(r), \nabla n(r)] = \int F_{xc}[n(r), \nabla n(r)] dr$$

The GGA method typically yields more accurate results than the LDA and is more commonly used in studies. In this method, the F_{xc} accounts for the necessary correction to the LDA exchange-correlation relation. Still, the exchange and correlation energy terms are calculated separately, with the exchange term being

$$E_x^{GGA}[n(r)] = \int \epsilon_x[n(r)] F_x^{GGA}(s) dr$$

where $F_x^{GGA}(s)$ is the exchange enhanced factor and s is a dimensionless reduced gradient. Multiple approximations for $F_x(s)$ exist, the most commonly used being the Perdew, Burke, and Ernzerhof (PBE) correlation, defined as

$$F_x^{PBE}(s) = 1 + k - \frac{\kappa}{1 + \frac{\mu s^2}{\kappa}}$$

where κ and μ are parameters determined by physical constraints. For more information on these exchange-correlation approximations see [45]. When we state that the GGA-PBE exchange-correlation was used, this means GGA is the exchange-correlation and PBE is the functional used for the DFT simulation. ATK, the software used for DFT simulations in this study, has multiple exchange-correlations and functionals beyond LDA, GGA, and PBE available.

The last component used in our DFT calculations is the pseudopotential approximation. Since valence electrons are primarily responsible for the chemical and electrical properties of most materials we are less interested in the core electrons which are more tightly bound to the nucleus. These core electrons require large basis sets for their description and greatly increase the computational cost of DFT calculations. We avoid this problem by using a pseudopotential approximation. This replaces the strong ionic potential of the core electrons with a weaker pseudopotential. This reduces both the number of calculations required to describe core electrons and the oscillation of valence electron wavefunctions (Figure 2.2). Significant research has gone into obtaining accurate pseudopotentials. One of the first popular sets of pseudopotentials was developed by Troullier and Martins in 1991 [46], followed by the more robust Hartwigsen-Goedecker-Hutter pseudopotentials in 1998 [47]. Recently, a more advanced approximation method known as projector-augmented wavefunctions (PAW), first proposed by Blochl in 1994 [48], has become a popular alternative to the pseudopotential method. In this study only Hartwigsen-Goedecker-Hutter (HGH) pseudopotentials were used for DFT calculations.

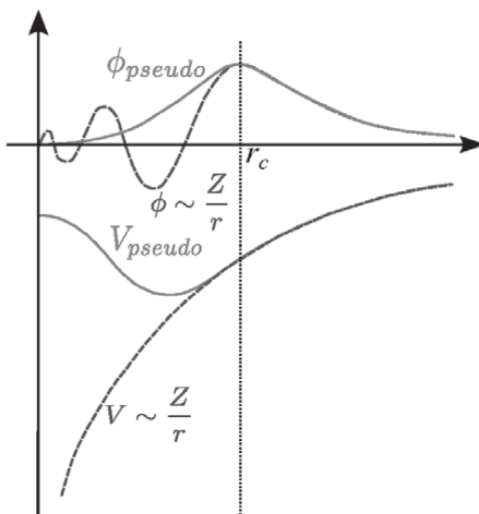


Figure 2.2: Pseudopotential approximation graphed with physical wavefunction. Outside the core radius the wavefunctions are identical [44].

2.3 ATK: Geometry Optimization and Bandstructure Calculations

All calculations performed in this study used the Quantumwise ATK 2015 software. Quantum ATK is an atomic scale modeling software which combines density functional theory with non-equilibrium Green's functions for large scale ab initio first principles calculations. First the geometry of each structure was optimized. This was done by first perturbing the atoms using the rattle tool to ensure the optimization converged to the global minimum. The ATK-DFT calculator with the GGA-PBE exchange-correlation functional was used in all simulations. A density mesh cutoff of 75 Hartree and 1x21x21 k-point sampling was used, as well as the HGH Tier 4 pseudopotential basis set. For geometry optimization FFT boundary conditions were used along with a force tolerance of 0.01 eV/Å, stress tolerance of 0.0005 eV/Å³ and a maximum step size of 0.5Å. The cell was constrained in the direction

normal to the surface of the sheet or nanoribbon (z direction for sheets, x direction for nanoribbons). For geometry optimization of the bilayer germanene van der Waals structure all constraints were released and the counterpoise correction with D2 dispersion correction was used (see [49]). The binding energy was calculated from the difference between the total energy of the bilayer system and the sum of the individual energies of the two germanene monolayers. For bandstructure calculations a vacuum of 15Å was added to each side of the structure to ensure decoupling from neighboring images. For bandstructure calculations of germanene nanoribbons Dirichlet boundary conditions were applied to the edges, while the normal and transport directions were set to periodic. Neumann boundary conditions were tested for the direction normal to the surface but produced identical results to periodic boundary conditions. 100 points per segment were used for all bandstructures. The geometries were analyzed by opening the .cif files in the Mercury molecular viewing software [50]. Band structures were analyzed in Quantumwise ATK 2015 band structure analyzer.

Chapter 3: Results

3.1 Mono-Layer Germanene Sheet

The results of geometry optimization reveal germanene to be a monolayer honeycomb lattice structure with 0.7\AA buckling. The lattice parameters obtained for the unit cell are $a = b = 4.07\text{\AA}$, with the primitive vectors being $a = b = 2.03\text{\AA}$. The Ge-Ge bond lengths are 2.45\AA and the total energy of the layer is -212.845 eV , all in good agreement with previous studies [16][18]. The DFT band structure calculations show a semimetal with the Dirac cone at the K point with valence and conduction bands coinciding at the Fermi level ($E = 0\text{ eV}$).

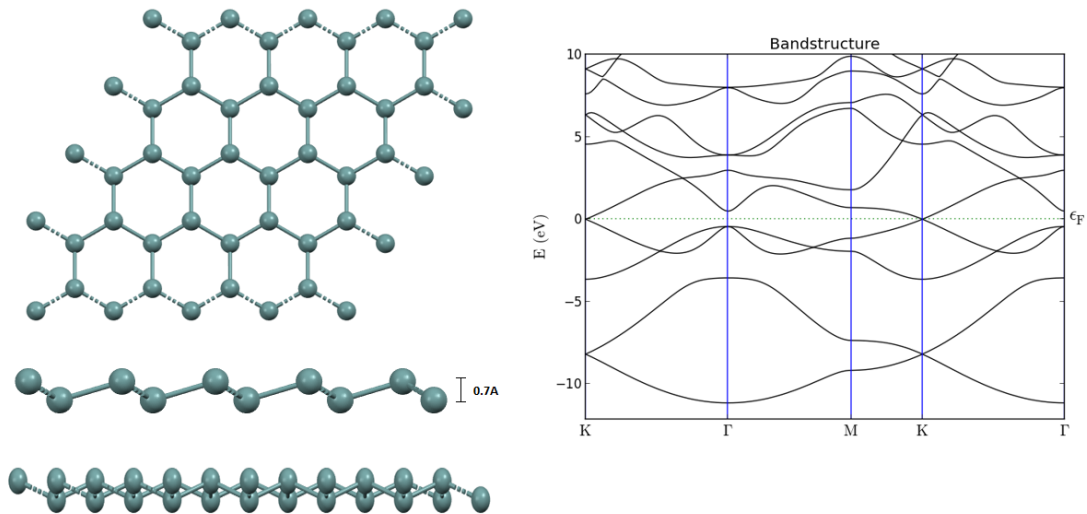


Figure 3.1: Germanene monolayer geometry and band structure. Material displays $\Delta = 0.7\text{\AA}$ buckling and band structure reveals a Dirac cone at the K point.

3.2 Bilayer Germanene van der Waals Structure

Like graphene, germanene should be able to form a multi-layer AA stacked van der Waals structure. The van der Waals force between the two layers binds them in place while keeping a separation distance sufficient to prevent Ge-Ge bonding between the two layers. Based on DFT geometry optimization, a stable bilayer van der Waals structure was obtained with a layer separation of 4.36\AA and a binding energy of -698.5 eV . The total energy of the structure is -1124.191 eV . Compared to bilayer graphene the band structure is more complex. It forms what would appear to be a nodal line semimetal with bands touching around the K point, however upon further inspection a non-trivial band gap is opened. This implies that as more germanene layers are stacked the band gap should continue to open until it reaches a limit around that of bulk germanium (0.67 eV). The electronic interaction between the layers demonstrates the importance of decoupling a single sheet from its periodic images when analyzing its band structure.

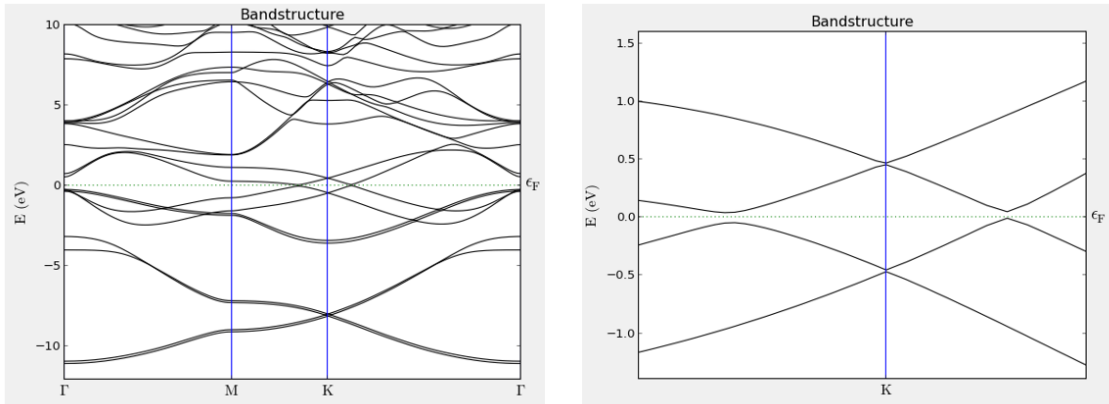


Figure 3.2: Band structure of bilayer germanene. Non-trivial opening of the band gap occurs as more layers are added.

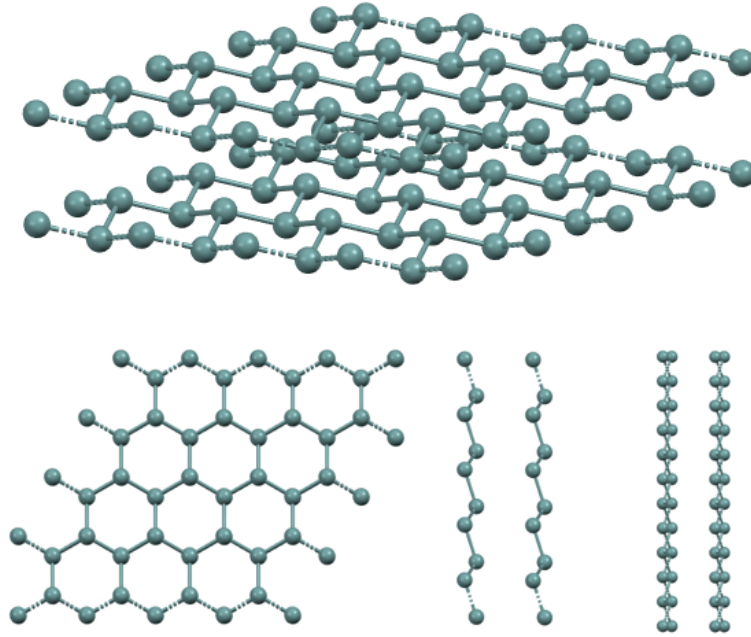


Figure 3.3: Geometry of Bilayer AA stacked germanene monolayers. Separation distance of 4.36\AA is maintained by van der Waals force.

3.3 Hydrogen Passivated Armchair Germanene Nanoribbon

As a base case we examined the effect of width on the band gap of the hydrogen passivated germanene armchair nanoribbon. The nanoribbon maintains the same 0.7\AA buckling as the germanene sheet with the hydrogen atoms placing themselves in between the two germanene planes. The band gap of the nanoribbon occurs at the Γ point as opposed to the K point in the germanene sheet. The band gap vs width relationship is cyclical with the pattern repeating every 3 atoms in width. It starts as a semiconductor in the 3-atom width case with a band gap of 0.738 eV , slightly higher than that of bulk Ge. The band gap then increases slightly in the 4-atom case before dropping to a near-trivial band gap of 0.045 eV at 5 atoms in width. As shown in Figure 3.5 the band gaps of the 3, 6 (3P) and 4

($3P + 1$) atom-width nanoribbons show clear semiconductor behavior with curved valence and conduction bands. However, the 5-atom case ($3P + 2$) shows a highly linear E-K relationship near the Γ point, indicating this nanoribbon may be a TSM and the small band gap that occurs is likely due to low resolution in the ATK program. Confirmation of semimetallic behavior is best determined by performing a local density of states (LDOS) calculation across the thickness of the nanoribbon. If a piling up of spin-up and spin-down states on opposing surfaces occurs, this provides a high level of certainty that the 5-atom width nanoribbon is indeed a semimetal. This result is known as the quantum spin Hall effect and is a standard property of both topological insulators and semimetals. ATK 2015 does not support this LDOS calculation and it is therefore outside the scope of this thesis. Nonetheless, a cyclical semiconductor-semiconductor-semimetal pattern appears to emerge, with the overall band gap decreasing logarithmically as width increases. This result shows good agreement with the results of Monshi et. al. and Shiraz et. al. [41][42].

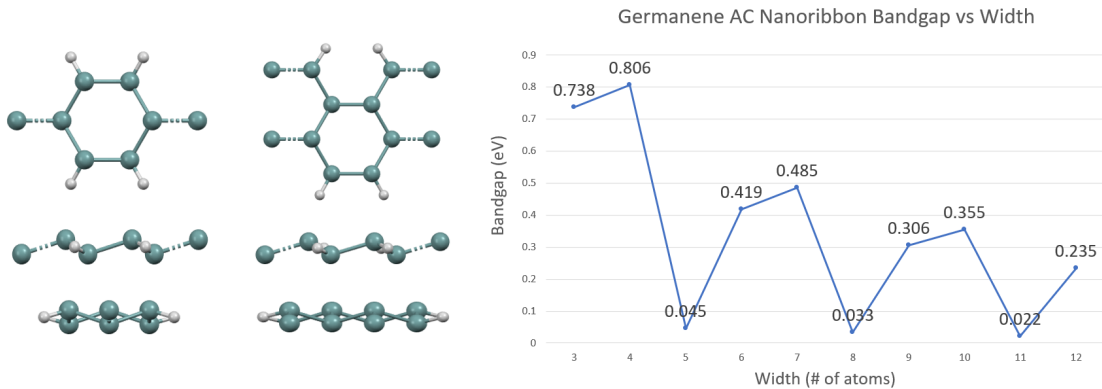


Figure 3.4: H-passivated Ge AC nanoribbons. The band gap vs width relationship shows a cyclical pattern where the $3P$ and $3P+1$ ribbons are semiconductors, with the $3P+1$ class having a higher average band gap. The $3P+2$ class shows semimetallic characteristics. The non-trivial band gap is likely a resolution error. The overall band gap decreases logarithmically maintaining the expected inverse relationship between band gap and width.

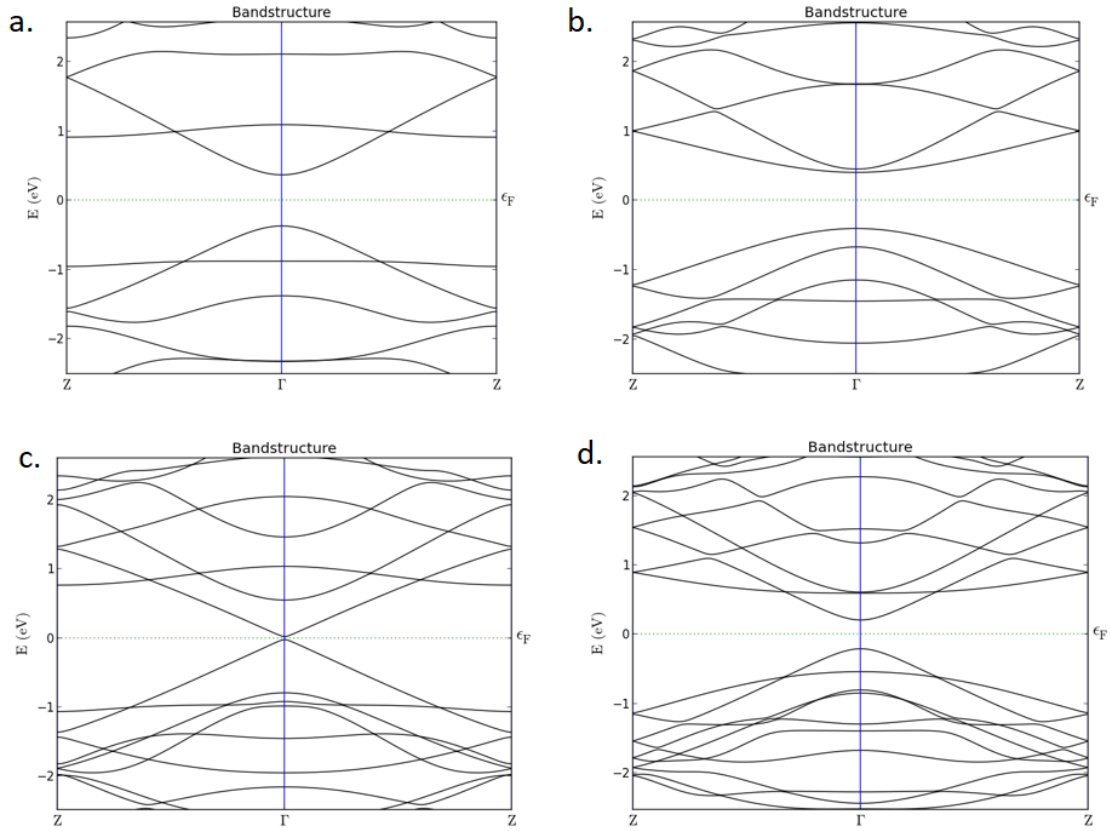


Figure 3.5: Band structures of 3 (a), 4 (b), 5 (c), and 6 (d) width Ge ACNRs. The 3P and 3P+1 class ribbons show a clear band gap while the 3P+2 (c) has a highly linear E-K relationship about the Γ point indicating semimetallic behavior.

3.4 Geometric Properties of Edge-Functionalized AC Ge Nanoribbons

A major component of this research is to build on the H-passivated nanoribbon results by examining the use of other species for edge-functionalization. While DFT calculations have been performed for the halogen group, little research has been done on the effect of the nonmetals (C, P, As, S, Se, and Te) on the band gap vs width behavior of Ge ACNRs. From this research we found striking differences in the behavior of these nanoribbons including

variations in their geometries. In the case of hydrogen and fluorine, since their outer valence shells consist of one and seven electrons respectively, the atoms only require one extra electron to fill their valence shell. Because of this, these two species fully passivate the Ge dangling bonds and create only one additional bond in the physical structure (Figure 3.6a). In the case of all other species examined in this thesis the edge atoms require more than one electron to fill their outer shell and thus form a bond with each other as well as the Ge atoms (Figure 3.6b). Even then, the valence shell of these atoms is not completely filled and it would be incorrect to refer to them as passivating the edge of the nanoribbon. Therefore we can refer to hydrogen and fluorine as edge-passivating while we refer to other species as edge atoms.

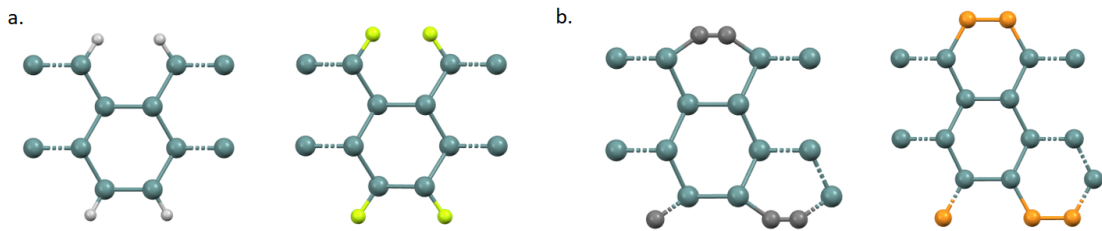


Figure 3.6: Different geometries of bonding between edge species. Hydrogen and fluorine (a) have a filled outer shell while other atoms (b, C on the left and P on the right) bond with each other.

Another geometric variation is where the foreign atoms lie with respect to the Ge planes. In the case of H, C, P, and As the edge atoms lie between the two displaced Ge lattices, where in the case of F, S, Se, and Te the atoms lie in plane with the two Ge lattices. In the latter case, the bond formed between the foreign species crosses over the Ge planes in the opposite direction of the Ge-Ge bond (Figure 3.7b). As the atomic weight of the species increases, the further out of plane the atoms become. In the case of sulfur the atoms are almost entirely in line with the Ge atoms, whereas in the case of selenium they protrude

slightly above the Ge plane and with tellurium the protrusion is highly noticeable (Figure 3.14).

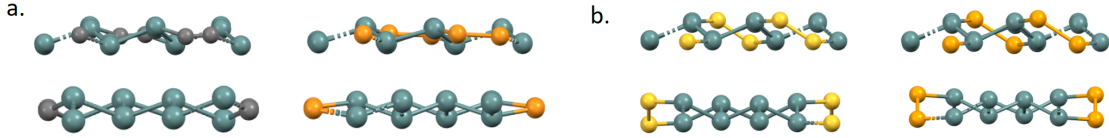


Figure 3.7: Placement of foreign atoms within the Ge lattice. H, C, P, and As place themselves between the Ge lattice (a, C left and P right) while F, S, Se, and Te place themselves in plane with the Ge atoms (b, S left and Se right).

Lastly, we note the existence of a bond inversion point in the nanoribbons at certain widths. In the example shown in figure 3.8b, the ACNRs with F and Se edge atoms show an inversion of bonds in the transport direction. This does not change the honeycomb structure from the planar view and is only visible from other vantage points. Each set of ACNRs analyzed in this study will undergo this inversion of bonds at certain widths, though no clear pattern emerged as to when this inversion will occur nor is there any obvious impact on the band structure.

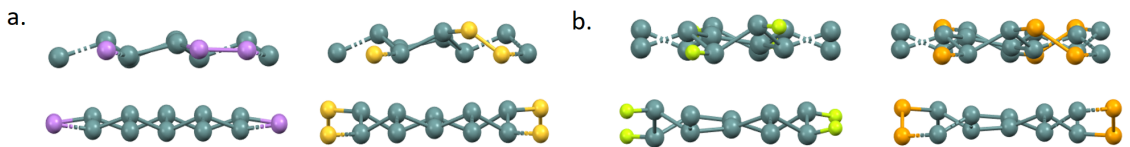


Figure 3.8: Example of bond inversion. At the 5-atom width, only F and Se exhibit this inversion (b). At different widths other Ge ACNRs will display this inversion.

3.5 Effect of Width on Band Gap of Edge-Functionalized AC Ge Nanoribbons

Each group of edge-functionalized Ge ACNRs show significant variability in their band gap vs width relationship, with none having as clear a cyclical relationship as the H-passivated case. With carbon (Figure 3.9), the band gap vs width follows an inverse relationship from that of hydrogen. Whereas the H-passivated group has a cyclical relationship of increasing twice before a large decrease in band gap, carbon has one increase followed by two decreases with no clear pattern in the relative magnitude of changes in band gap. It starts with a 0.672 eV band gap in the 3-atom case and decreases down to 0.201 eV for the 5-atom ribbon. It then varies in a small range where the 6-atom and 9-atom ribbons have similar band gaps of 0.428 eV and 0.41 eV respectively before falling to a near-trivial band gap at 11 atoms in width. The band structure for the 11-atom case shows the same highly linear E-K relationship as in the 5, 8, and 11-atom width hydrogen nanoribbons, implying semimetallic behavior. The C-C bonds formed between the carbon atoms are the smallest bonds of all edge species observed in this thesis. This leads to an elongated Ge-Ge bond in the width direction whereas the other nanoribbons are more uniform in their hexagonal Ge structures.

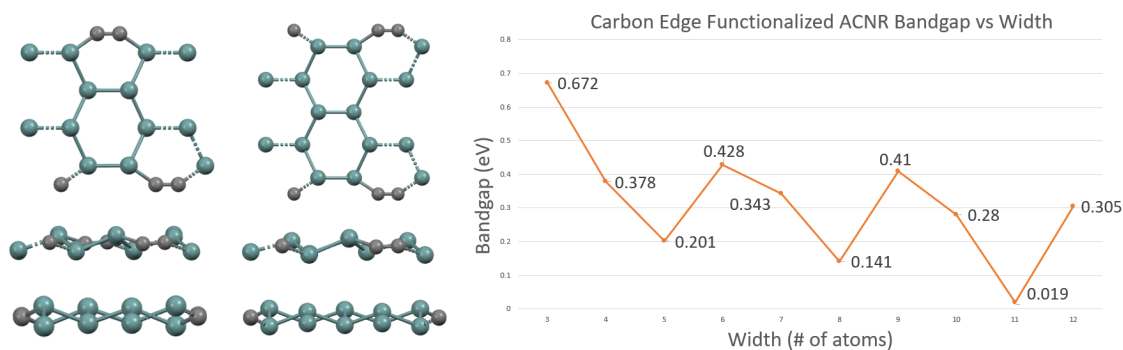


Figure 3.9: C edge-functionalized Ge ACNR (left) and band gap vs width relationship (right)

Phosphorus and arsenic ACNRs show similarities in their width vs band gap behavior differentiating them from the other nanoribbons. In both groups we see a sharp increase in band gap from 3 to 5 atoms in width before a steep decline to a lower band gap in the 6-atom case. Both then show a trapazoidal square wave-like relationship from 6 to 11 atoms in width before dropping to a near-trivial band gap at the 12-atom case. Geometrically, both phosphorus and arsenic place themselves between the Ge atoms and form relatively symmetric honeycombs with similar Ge-Ge bond lengths. The band gap vs width relationship shows a more linear decrease in peaks than that of the H-passivated case, which is logarithmic.

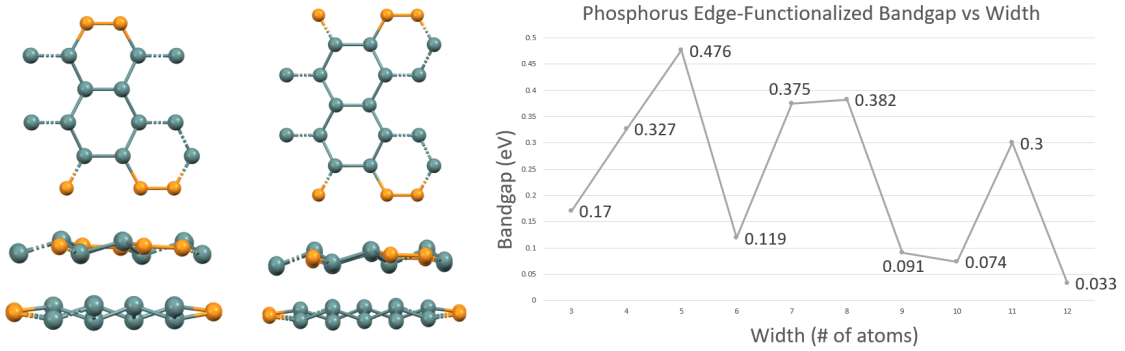


Figure 3.10: P edge-functionalized Ge ACNR (left) and band gap vs width relationship (right)

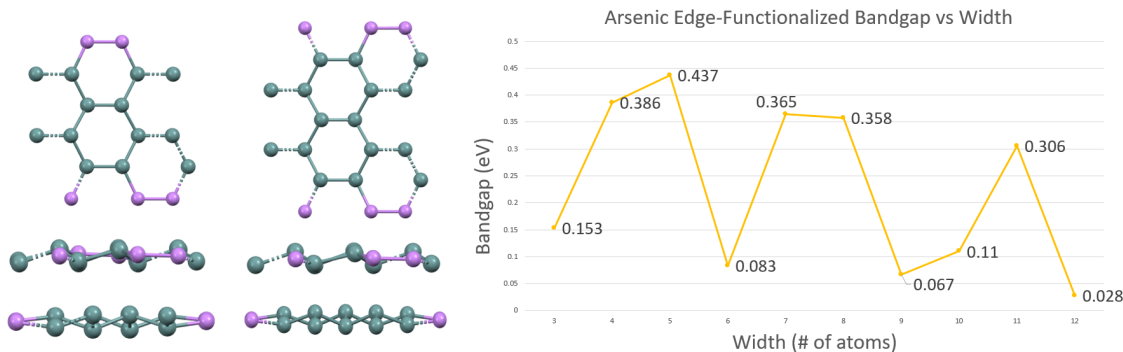


Figure 3.11: As edge-functionalized Ge ACNR (left) and band gap vs width relationship (right)

Sulfur and selenium ACNRs also share distinctions from the other ribbons. In both groups the foreign atoms lie in plane with the Ge atoms with far less protrusion than in the tellurium ACNRs. Their band gap vs width relationship is defined by sharp peaks and troughs, with the 8 and 11-atom width nanoribbons having around 0.3 eV band gap for both groups. For both 9 and 12 atoms in width the band gap is near-trivial and displays a linear E-K relationship around the Γ point. There are notable differences between the two as well; the sulfur nanoribbons show an increase in band gap from 6 to 7 atoms in width whereas the selenium nanoribbons decrease, and the 10-atom sulfur ribbon has roughly 1.5x the band gap (0.236 eV) of its selenium counterpart (0.168 eV). Nonetheless both achieve their first peak at around 0.38 eV (4-atom width for sulfur and 5 for selenium) and both have similarities at the 8 and 11-atom widths as well as semimetallic behavior at 9 and 12 atoms in width. It is worth noting that sulfur forms the smallest bond between edge atoms after carbon, but unlike carbon this does not lead to a noticeable distortion in Ge-Ge bond length.

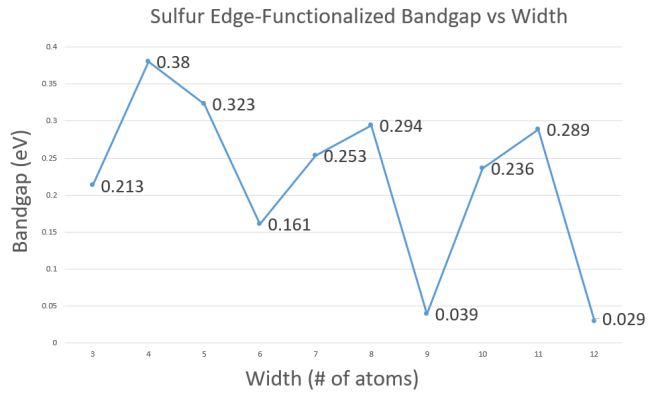
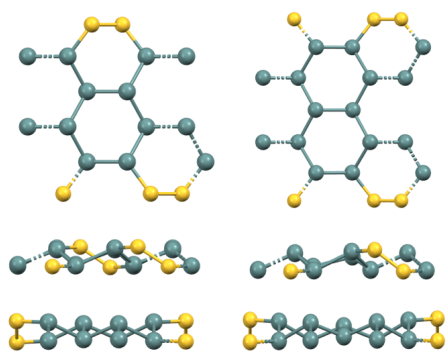


Figure 3.12: S edge-functionalized Ge ACNR (left) and band gap vs width relationship (right)

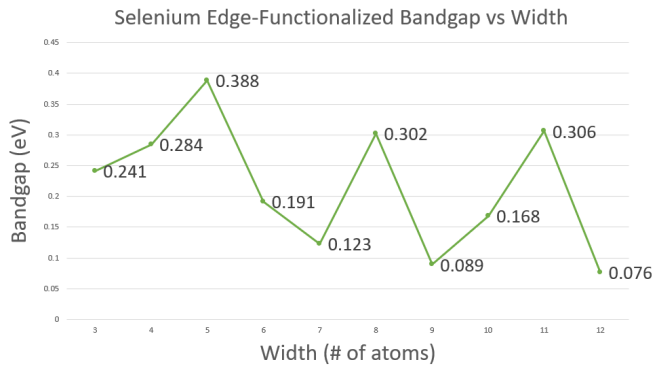
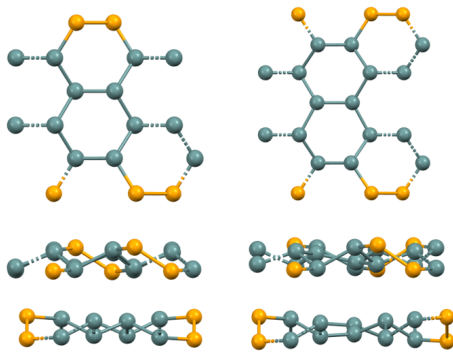


Figure 3.13: Se edge-functionalized Ge ACNR (left) and band gap vs width relationship (right)

The tellurium nanoribbons are unique among the groups. Geometrically the Te atoms protrude noticeably outside the Ge planes while the Ge-Ge bonds are highly symmetric. However the band gap vs width relationship bears the most similarity with the H-passivated case. The band gap increases greatly from 0.267 eV to 0.754 eV for the 3 to 4-atom widths before dropping to a near-trivial band gap at the 5-atom width. It then shows a similar

pattern to that of hydrogen, having a cyclical 3 width pattern of increasing band gaps as a semiconductor before dropping to a near-trivial band gap with semimetallic behavior at 5, 8, and 11 atoms in width. It is worth noting that unlike the H-passivated ribbons, the band gaps of the 6, 7, 9, and 10-atom Te ribbons fall in a more narrow range, and a dropoff occurs at the 12-atom point with a band gap of 0.145 eV as opposed to 0.239 eV and 0.218 eV in the 6 and 9-atom cases.

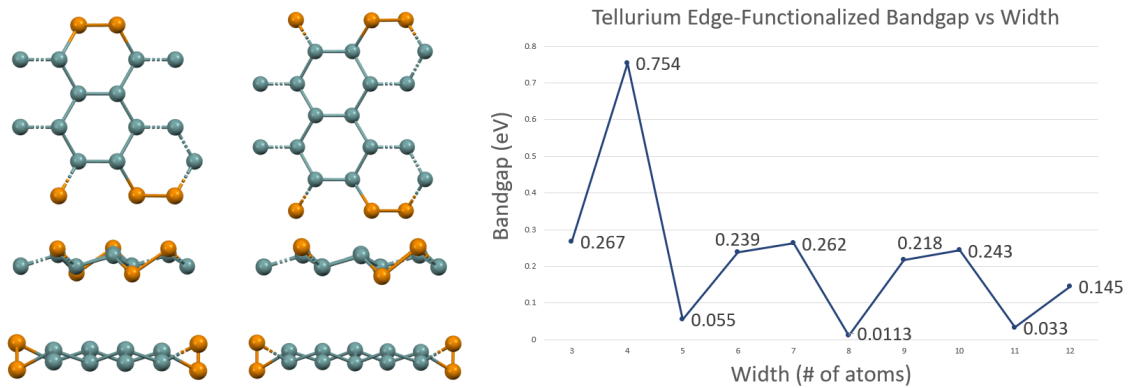


Figure 3.14: Te edge-functionalized Ge ACNR (left) and band gap vs width relationship (right)

Lastly, we address the case of the halogens. Previous work on the band gap vs width relationship of F and Cl as edge species for Ge ACNRs was carried out by Monshi et. al. using ATK 2014 [41]. However, using their same methods in ATK 2015 produced different results. The fluorine passivated nanoribbons only achieved stability as symmetric honeycombs for the 4 through 8-atom width ribbons. Both in the 3-atom case and for widths of 9 atoms or greater the Ge-Ge bonds lose symmetry. This behavior is more noticeable in the case of the bromine and iodine nanoribbons (Figure 3.16). For fluorine, our results show a relationship akin to the Te and H-passivated ACNRs: the largest band gap being at 4 atoms in width (0.837 eV), a near-trivial band gap at 5 and 8 atoms in width, and showing semiconductor behavior at 6 and 7 atoms in width. If a stable configuration can

be achieved for greater than 8 atoms, we predict a similar cyclical 3 width pattern with semimetallic behavior at 11 atoms in width. In the case of the remaining halogens, no symmetric honeycomb structure was obtained. While the 3-atom width Cl ribbon appears symmetric from the transport direction vantage point, when examining the structure closely from the planar view the Ge-Ge bonds all show slight variation in length. This distortion becomes more pronounced as width increases. In the case of bromine and iodine, significant distortion of the hexagonal structure can be seen from the transport direction vantage point. We hypothesize this may be due to the high electronegativity of these foreign atoms. The chlorine, bromine, and iodine atoms will not be fully passivated from the additional Ge bond as in the fluorine case, and thus wish to form additional σ -bonds with the remaining Ge atoms leading to this distortion. The band structures for the 3-atom width Cl, Br, and I nanoribbons bear the following similarities: they show semiconductor behavior with band gaps of 0.538 eV, 0.541 eV, and 0.511 eV respectively, and they all show curved conduction bands but relatively flat valence bands. Stable configurations for halogen edge species may be obtainable by doubly passivating the Ge atoms at the edge. By passivating the fourth dangling Ge bond, it is no longer available for bonding with the halogen atom and may therefore prevent distortion, while the edge species may form additional bonds with each other instead. More research should be conducted on the stability of the halogen group as edge species, as the band gap obtained from the 3-atom width structures covers a range not found in the other groups (0.5 eV - 0.6 eV).

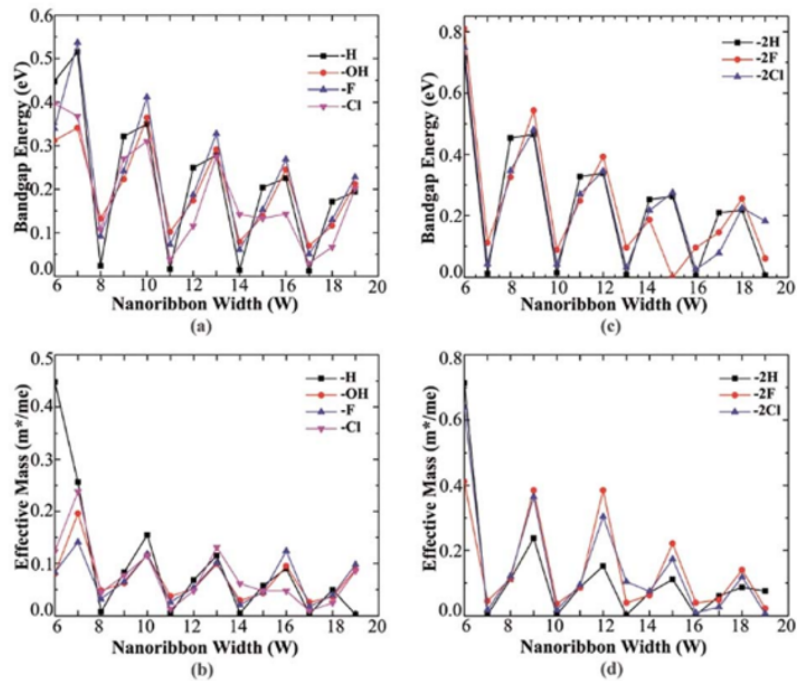
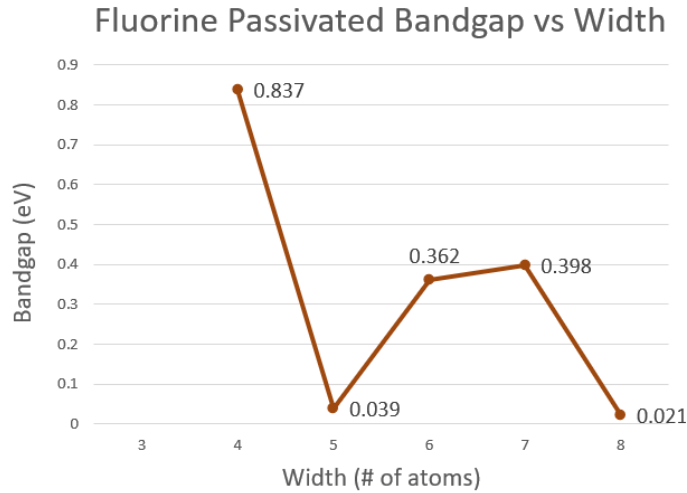


Figure 3.15: Results from this study for fluorine passivation (left) compared to Monshi et al. (right). Using the same parameters described in their paper we were unable to obtain the same results for F-passivation while our H-passivated nanoribbons show good agreement. Monshi's F-passivated nanoribbons show similar cyclical behavior to H-passivated with $3P+2$ ribbons being semimetallic, however there is a larger difference in band gap between $3P$ and $3P+1$ ribbons. Our F-passivated ribbons show a more similar pattern to H-passivation for $3P$ and $3P+1$ widths.

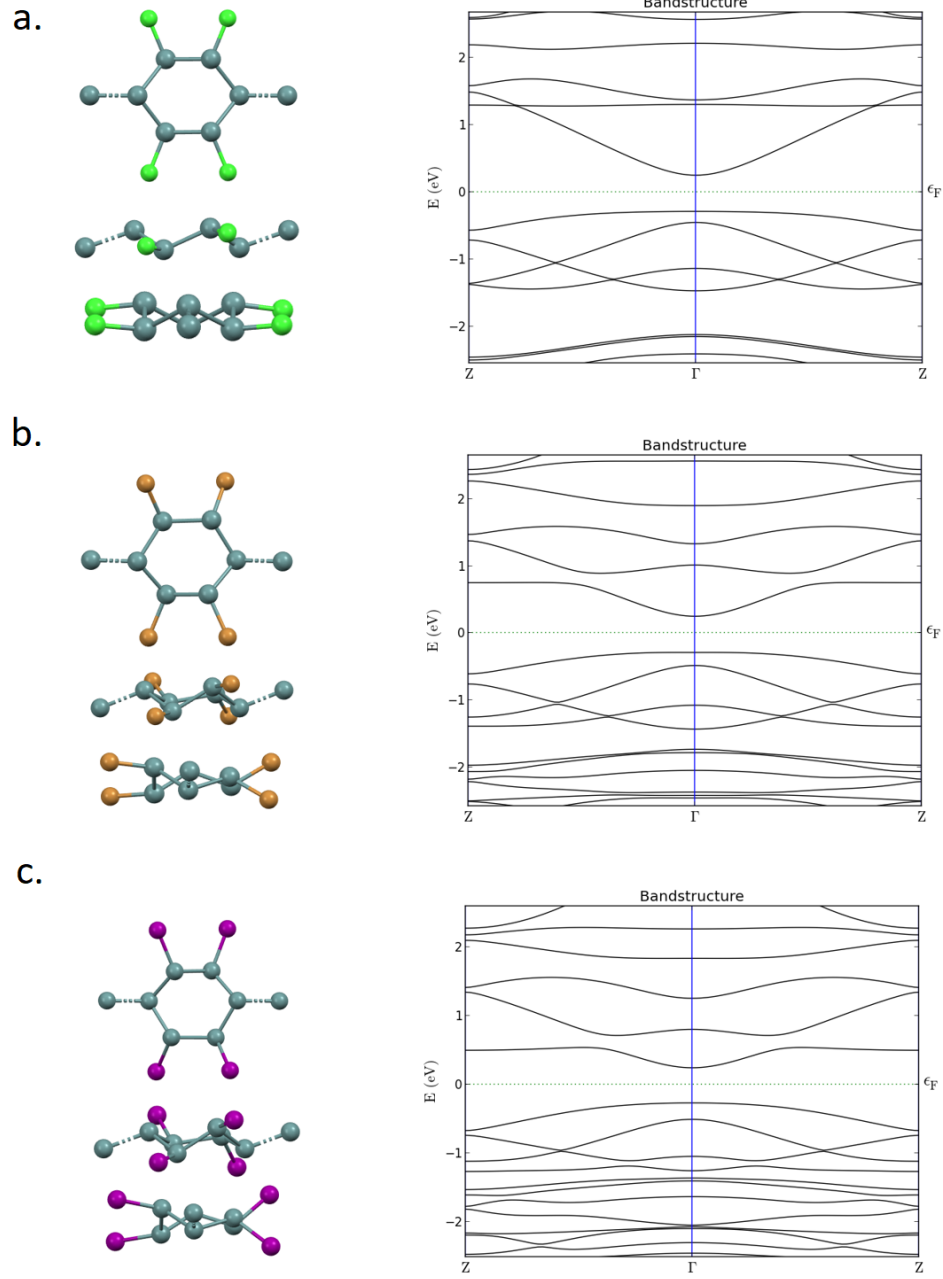


Figure 3.16: Results from this study for the halogen edge group of Ge ACNRs. From top to bottom: Cl, Br, and I. The Ge-Ge bonds are uneven and the band structures show a curved conduction band with a flat valence band and noticeable band gap. In the case of Br and I nanoribbons significant distortion of the lattice can be seen in the transport direction.

3.6 Effect of Strain on H-Passivated Ge ACNR Band Structure

The application of strain to adjust the band gap of graphene has been well studied. Shiraz. et. al. analyzed the effect of strain in the transport direction on the band gap of 9, 10, and 11-atom width H-passivated Ge ACNRs [42]. In this study we repeated his results and expanded them to a 10% strain case, as well as examined the effects of applying strain in the longitudinal (width) direction. We also performed calculations for 0.1% - 0.5% strain to analyze the resolution of strain application for fine tuning of the band gap. The %strain vs band gap relationship varies substantially for each class of nanoribbon. The band gap in the lateral case can be tuned to a maximum of 0.5 eV, 0.45 eV, and 0.4 eV for the 9, 10, and 11-atom width nanoribbons respectively. The band gap for each can also be closed to a near-trivial value with linear dispersion around the Γ point. In the case of longitudinal strain the maximum band gap for the 9-atom case is higher at 0.55 eV, while similarly each can be tuned to a near-trivial band gap. While application of 0.1% - 0.5% strain results in minimal change in band gap, this change is continuous thus allowing for high resolution tuning.

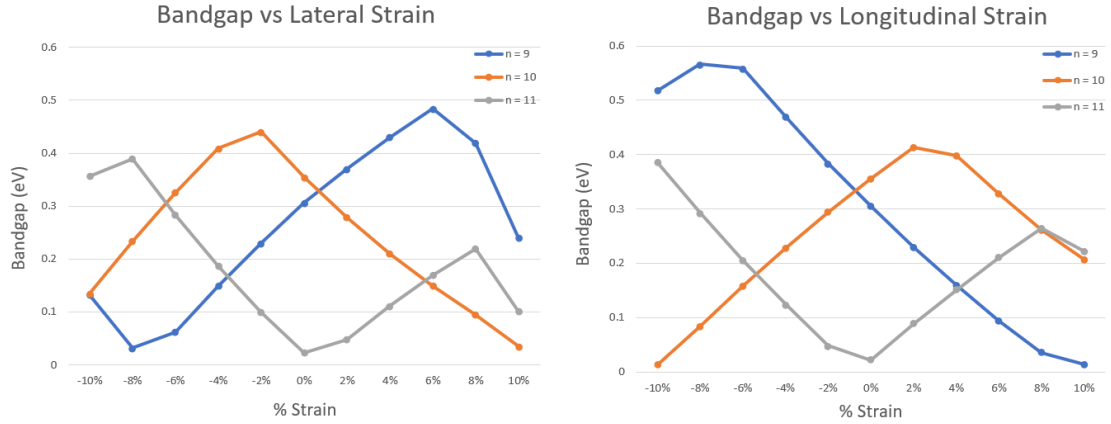


Figure 3.17: Band gap vs % strain for 3P, 3P+1, and 3P+2 class H-passivated Ge ACNRs. Results for lateral strain match well with Shiraz et. al.

3.7 H-passivated Zigzag Germanene Nanoribbons

The nature of ZZ germanene nanoribbons appears to differ substantially from that of their AC counterparts. Geometrically they are quite similar, both demonstrate the same 0.7\AA buckling and maintain the same 2.45\AA bond length. The hydrogen atom also places itself between the two Ge planes. However, the band gaps in the H-passivated ZZNRs reveal nodal line semimetals. A change in the width adjusts the shape of the Dirac surface but no band gap is opened. In the 4-atom case the Dirac surface forms a single loop, where the trivial band gap that appears in the band structure diagram is likely a resolution error. When the width is increased to 6 atoms two loops appear, and in the 8-atom case a lopsided single loop forms. Based on the results of Matthes and Sharma [39][40] we predict that as the width increases the gap will close leading to a dense line of degenerate states at the edges as seen in Figure 1.8a. To our knowledge, previous studies have not examined the case of low width ZZ nanoribbons ($m = 4, 6, \text{ and } 8$) and this thesis is the first to report nodal line semimetal characteristics in Ge nanoribbons.

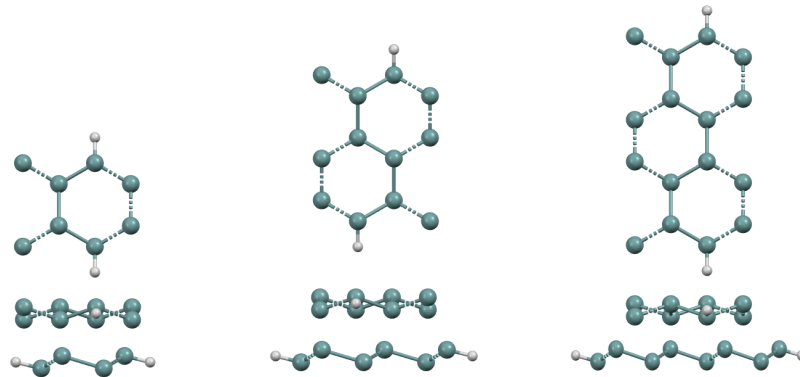


Figure 3.18: Geometry of Ge ZZNRs of various widths. The H-passivated nanoribbons maintain the same 0.7\AA buckling and placement of hydrogen atoms.

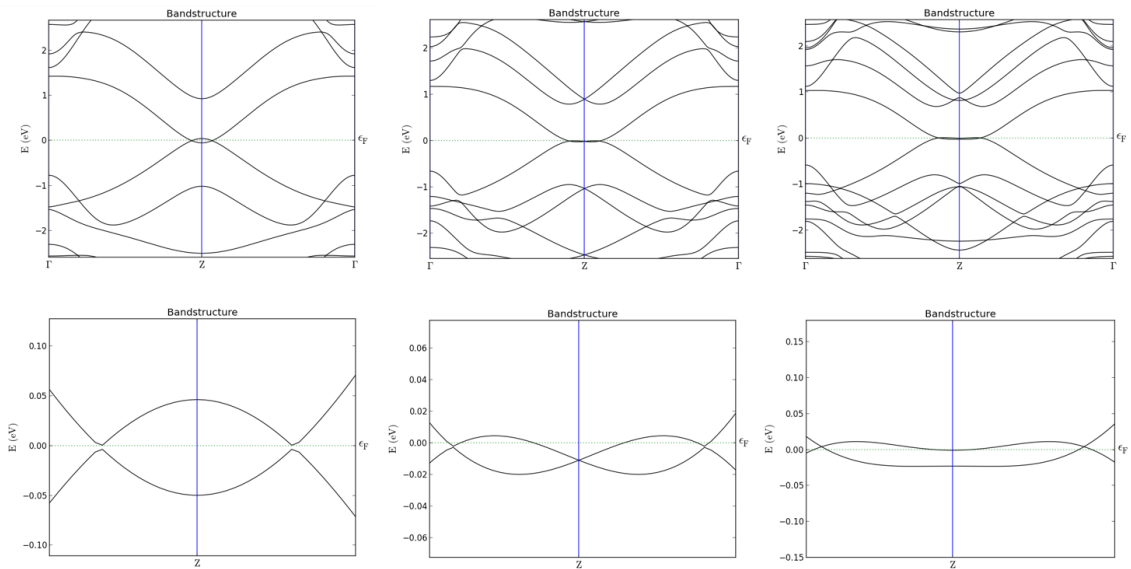


Figure 3.19: From left to right: band structure of 4, 6, and 8-atom width H-passivated Ge ZZNRs. The 4-atom band structure reveals a nodal semimetal with a single looped Fermi surface, the 6-atom has a double looped Fermi surface and the 8-atom case has a single loop but with a downward bending conduction band. As width increases the conduction band will likely bend into the valence band resulting in metallic behavior.

3.8 Edge-Functionalized ZZ Ge Nanoribbons

An examination of edge-functionalized species on Ge ZZNRs was performed for this thesis. The species which form symmetric honeycomb configurations differ from those of the ACNRs; for example carbon does not form a hexagonal structure and folds into a 3-dimensional shape whereas chlorine forms a symmetric hexagonal structure. In each ZZNR the foreign atom places itself between the Ge atoms with its bond parallel in the width direction. There is however a geometric variation among the Ge atoms in the transport direction: they either alternate between lying in two separate planes and overlapping in a single intermediate plane with the foreign atom (Figure 3.20a), or continue to criss-cross between the two Ge planes as seen in the ACNRs (Figure 3.20b). The alternating structure results from P, As, S, Se, and Te ZZNRs, while the symmetric structure results from H, F, and Cl.

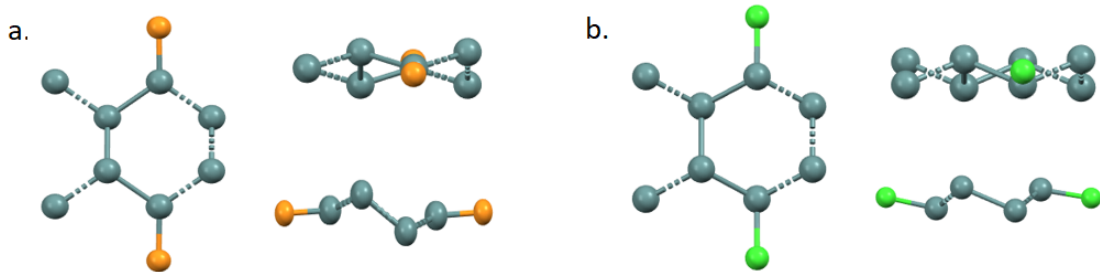


Figure 3.20: Edge functionalized Ge ZZNRs. Geometrically they fall into two classes: alternating structure (a) where every other Ge atom overlaps as seen with P, As, S, Se, and Te, and symmetric structure (b) where the Ge atoms remain in separate planes as seen in H, F, and Cl.

The resulting band structures of these nanoribbons fall into three categories which are not predicted by the geometry. In the first case a nodal line semimetal with a single loop around the Γ point forms. This is seen in the case of hydrogen and sulfur (Figure 3.21a), where the sulfur band structure has a lopsided loop protruding more in the conduction band than the valence band. In the case P, As, Se, and Te we have a valence band that

protrudes well above the Fermi level to make contact with the conduction band, though the bands simply touch and do not cross. Lastly, in the case of F and Cl the bands have a minimum at the Z point. While it appears like they touch, we judge this structure to be a very narrow-band gap semiconductor as the E-K relationship is highly non-linear. Applications and properties of nodal line semimetals are complex and beyond the scope of this thesis. Further research into these zigzag nanoribbons may reveal potential applications in spintronics or as superconductors due to their electronic and magnetic properties. For further information see [39][40].

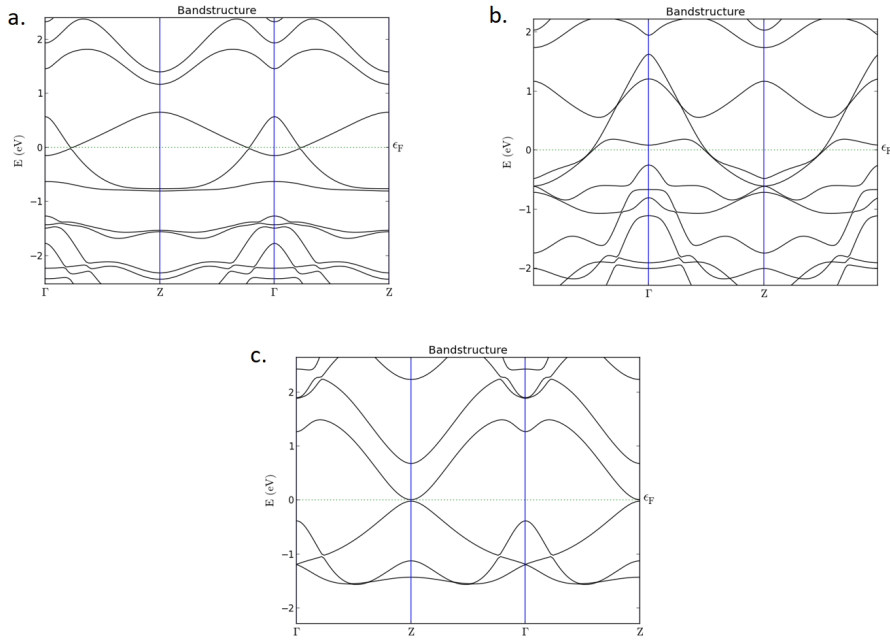


Figure 3.21: Band structures of various edge species on Ge ZZNRs. (a) Nodal line semimetal behavior about the Γ point (H, S), (b) valence band protruding above the Fermi level making contact with the conduction band (P, As, Se, Te), (c) narrow band gap semiconductor with near trivial band gap but highly non linear E-K relationship (F, Cl).

Chapter 4: Discussion and Future Research

Free-standing monolayer germanene forms a buckled honeycomb structure exhibiting semimetallic behavior with a Dirac cone at the K point. We confirmed results of previous studies both with the 0.7Å buckling height and the location of the Dirac point. Bilayer AA stacked germanene forms a van der Waals structure with a small opening of the band gap and a layer separation of 4.36Å. The edge-functionalized ACNRs vary significantly in their band gap vs width behavior. When graphed together (Figure 4.1) we begin to see relationships between the different groups. They appear to form three groupings: H, F, and Te form the first group, followed by As, P, S, and Se, and lastly the halogens Cl, Br, and I for the single point calculated. The carbon ACNRs appear to follow a unique pattern, likely due to the elongated vertical Ge-Ge bond lengths. In the first group we see a large band gap varying from 0.75 eV to 0.85 eV at 4 atoms in width, with F having the largest. They then follow a 3-width cyclical pattern, display semimetallic behavior at 5, 8, and 11-atom widths, and show larger band gaps in the 3P+1 class than the 3P class of ACNRs. As, P, S, and Se all group relatively close to each other throughout with the 7-atom Se ACNR being the sole outlier. As width increases these groupings become more pronounced. At 11 atoms in width the two groups split with members of each having nearly identical band gaps. When considering the energy gaps of all ACNR permutations examined in this thesis, they nearly span the entire IR spectrum. Coupled with the high tunability of Ge ACNRs through strain engineering it may be possible to create detectors for any IR spectral band. Currently this feat has only been achieved with HgCdTe technology. While germanene monolayers are shown to have strong absorption throughout the IR spectrum, such studies have yet to be performed on Ge ACNRs.

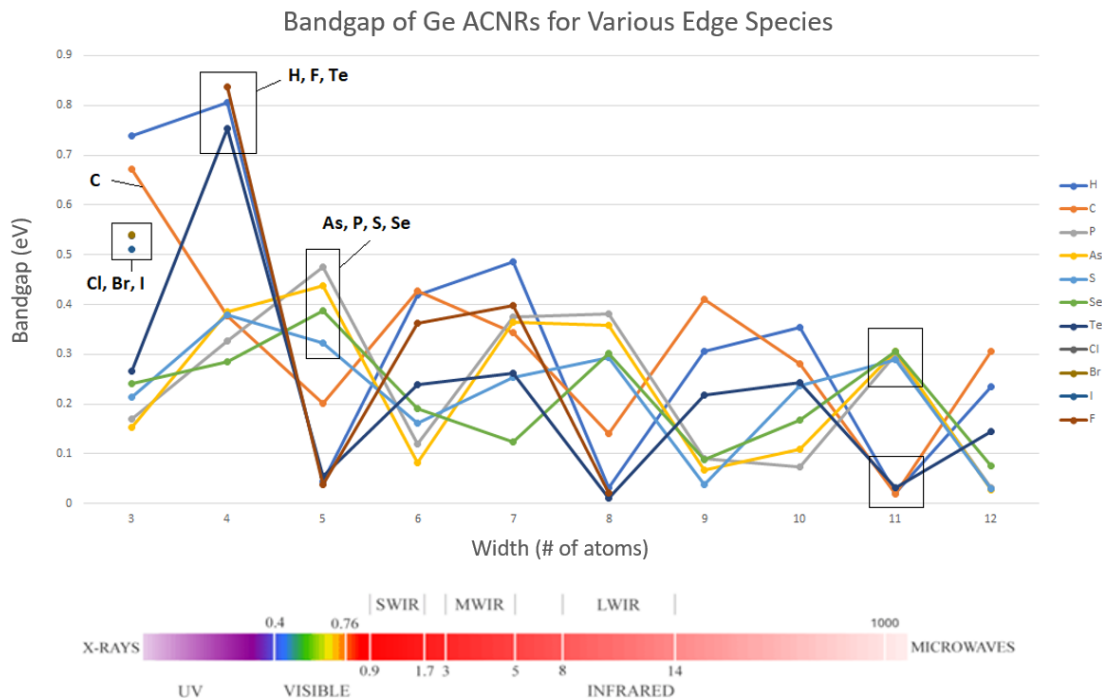


Figure 4.1: Plot of band gap vs width for various edge-functionalized Ge ACNRs. The different edge species appear to form 3 distinct groupings with the carbon nanoribbons as the outlier. The total set of band gaps spans the IR spectrum.

Low width ($m = 4, 6, 8$) H-passivated Ge ZZNRs are revealed to be nodal semimetals. As the width increases the conduction band begins to bend towards the valence band. Unlike their AC counterparts, chlorine forms a stable 2D structure in ZZNRs whereas carbon does not. These nanoribbons display three distinct band structures: nodal semimetal (H, S), valence band protruding above the Fermi level (P, As, Se, Te), and extremely narrow band gap semiconductor with non linear band dispersion (F, Cl). Further studies on the effects of width on Ge ZZNRs should be explored as well as confirming magnetic properties of the edge states. LDOS vs thickness calculations should be carried out on the Ge ACNRs to confirm semimetallic behavior by demonstration of the quantum spin Hall effect. Absorption spectra calculations on the ACNRs should also be examined to see if they have potential applications as IR sensors.

Chapter 5: Conclusion

In this thesis we confirmed the results for free-standing monolayer germanene as well as H-passivated Ge ACNRs using DFT first principle calculations. We then explored edge-functionalization of Ge ACNRs and ZZNRs across various widths, as well as established the formation of a van der Waals bilayer AA structure formed from Ge monolayers and the effect of strain on band gap tuning of Ge ACNRs. We confirmed that monolayer germanene is a buckled semimetal with a Dirac cone at the K point and that the Ge bilayer structure has a non-trivial band gap and separation distance of 4.36\AA . We found the same cyclical relationship between band gap and width for H-passivated Ge ACNRs as established by Monshi et. al. and Shiraz et. al. where the $3P$ and $3P+1$ classes are semiconducting while the $3P+2$ class displays a linear E-K relationship and is likely semimetallic. We noted the distinct geometric and electronic groups formed from the different edge-functionalized ACNRs, whose band gaps in total nearly span the entire IR spectrum, ranging from near-trivial to 0.837 eV . The band gaps are highly tunable through the application of strain in either the transport or longitudinal (width) direction. We also note the lack of structural stability in the halogen group of Ge ACNRs. Notably, we recognized the existence of Fermi surfaces in low width H-passivated Ge ZZNRs, particularly the 4-atom width case which presents the band structure of a looped nodal line semimetal. We noted the downward bending of the conduction band as width increased as well as the differences in stability between edge species for ZZNRs and ACNRs. We found the edge-functionalized ZZNRs have three distinct band structures none of which bear similarity to the ACNR band structures. We recommend analysis of the absorption spectra of Ge ACNRs for potential use as IR sensors as well as LDOS vs thickness calculations to confirm semimetallic behavior in near-trivial band gap nanoribbons.

Bibliography

Bibliography

- [1] L. Madkour, *Nanoelectronic Materials, Fundamentals and Applications*, 1st ed. Cham, Switzerland: Springer, January 2019, ch. 1, p. 4.
- [2] (2021, November) The graphene flagship. The European Union. Graphene-flagship.eu. [Online]. Available: <https://graphene-flagship.eu/collaboration/about-us/the-graphene-flagship/>
- [3] (2021, November) About the nni. National Nanotechnology Coordination Office. nano.gov. [Online]. Available: <https://www.nano.gov/about-nni>
- [4] H. Dong, Y. Gao, and P. Sinko. (2016, April) The nanotechnology race between china and usa. materialstoday.com. [Online]. Available: <https://www.materialstoday.com/nanomaterials/comment/the-nanotechnology-race-between-china-and-usa/>
- [5] R. Peierls, “Quelques propriétés typiques des corps solides,” *Annales de l’institut Henri Poincaré*, vol. 5, no. 3, pp. 177–222, 1935. [Online]. Available: http://www.numdam.org/item/AIHP_1935__5_3_177_0/
- [6] L. D. Landau, “Zur theorie der phasenumwandlungen ii,” *Phys. Z. Sowjetunion*, vol. 11, no. 545, pp. 26–35, 1937.
- [7] P. R. Wallace, “The band theory of graphite,” *Phys. Rev.*, vol. 71, pp. 622–634, May 1947. [Online]. Available: <https://link.aps.org/doi/10.1103/PhysRev.71.622>
- [8] D. P. DiVincenzo and E. J. Mele, “Self-consistent effective-mass theory for intralayer screening in graphite intercalation compounds,” *Phys. Rev. B*, vol. 29, pp. 1685–1694, Feb 1984. [Online]. Available: <https://link.aps.org/doi/10.1103/PhysRevB.29.1685>
- [9] (2021, November) The nobel prize in physics 2010. Nobel Prize Outreach. nobelprize.org. [Online]. Available: <https://www.nobelprize.org/prizes/physics/2010/summary/>
- [10] D. Zhan, J. Yan, L. Lai, Z. Ni, L. Liu, and Z. Shen, “Engineering the electronic structure of graphene,” *Advanced Materials*, vol. 24, no. 30, pp. 4055–4069, 2012. [Online]. Available: <https://onlinelibrary.wiley.com/doi/abs/10.1002/adma.201200011>
- [11] L. M. Schoop, F. Pielhofer, and B. V. Lotsch, “Chemical principles of topological semimetals,” *Chemistry of Materials*, vol. 30, no. 10, p. 31553176, Apr 2018. [Online]. Available: <http://dx.doi.org/10.1021/acs.chemmater.7b05133>

- [12] L. jing Yin, K. ke Bai, W. xiao Wang, S.-Y. Li, Y. Zhang, and L. He, “Landau quantization of dirac fermions in graphene and its multilayer,” *Frontiers in Physics*, vol. 12, no. 127208, April 2017. [Online]. Available: <https://link.springer.com/article/10.1007/s11467-017-0655-0#article-info>
- [13] A. H. Castro Neto, F. Guinea, N. M. R. Peres, K. S. Novoselov, and A. K. Geim, “The electronic properties of graphene,” *Reviews of Modern Physics*, vol. 81, no. 1, p. 109162, Jan 2009. [Online]. Available: <http://dx.doi.org/10.1103/RevModPhys.81.109>
- [14] F. Utermohlen. (2018, September) Tight-binding model for graphene. Ohio State University. [Online]. Available: https://cpb-us-w2.wpmucdn.com/u.osu.edu/dist/3/67057/files/2018/09/graphene_tight-binding_model-1ny95f1.pdf
- [15] C. Bouhafs, “Structural and electronic properties of graphene on 4h- and 3c-sic,” Ph.D. dissertation, Linkping University, Department of Physics, Linkping, Sweden, November 2016.
- [16] M. Ezawa, “Monolayer topological insulators: Silicene, germanene, and stanene,” *Journal of the Physical Society of Japan*, vol. 84, no. 12, p. 121003, Dec 2015. [Online]. Available: <http://dx.doi.org/10.7566/JPSJ.84.121003>
- [17] G. R. Yazdi, T. Iakimov, and R. Yakimova, “Epitaxial graphene on sic: A review of growth and characterization,” *Crystals*, vol. 6, no. 5, 2016. [Online]. Available: <https://www.mdpi.com/2073-4352/6/5/53>
- [18] A. Acun, L. Zhang, P. Bampoulis, M. Farmanbar, A. van Houselt, A. N. Rudenko, M. Lingenfelder, G. Brocks, B. Poelsema, M. I. Katsnelson, and H. J. W. Zandvliet, “Germanene: the germanium analogue of graphene,” *Journal of Physics: Condensed Matter*, vol. 27, no. 44, p. 443002, oct 2015. [Online]. Available: <https://doi.org/10.1088/0953-8984/27/44/443002>
- [19] K. Khan, A. K. Tareen, M. Aslam, R. Wang, Y. Zhang, A. Mahmood, Z. Ouyang, H. Zhang, and Z. Guo, “Recent developments in emerging two-dimensional materials and their applications,” *J. Mater. Chem. C*, vol. 8, pp. 387–440, 2020. [Online]. Available: <http://dx.doi.org/10.1039/C9TC04187G>
- [20] P. Vogt, P. De Padova, C. Quaresima, J. Avila, E. Frantzeskakis, M. C. Asensio, A. Resta, B. Ealet, and G. Le Lay, “Silicene: Compelling experimental evidence for graphenelike two-dimensional silicon,” *Phys. Rev. Lett.*, vol. 108, p. 155501, Apr 2012. [Online]. Available: <https://link.aps.org/doi/10.1103/PhysRevLett.108.155501>
- [21] E. Cinquanta, E. Scalise, D. Chiappe, C. Grazianetti, B. van den Broek, M. Houssa, M. Fanciulli, and A. Molle, “Getting through the nature of silicene: An sp²sp³ two-dimensional silicon nanosheet,” *Journal of Physical Chemistry C*, vol. 117, pp. 16 719–16 724, 2013.
- [22] J. Yuhara, B. He, N. Matsunami, M. Nakatake, and G. Le Lay, “Graphene’s latest cousin: Plumbene epitaxial growth on a nano watercube,” *Advanced Materials*, vol. 31, no. 27, p. 1901017, 2019. [Online]. Available: <https://onlinelibrary.wiley.com/doi/abs/10.1002/adma.201901017>

- [23] Z.-G. Shao, X.-S. Ye, L. Yang, and C.-L. Wang, “First-principles calculation of intrinsic carrier mobility of silicene,” *Journal of Applied Physics*, vol. 114, no. 9, p. 093712, 2013.
- [24] X.-S. Ye, Z.-G. Shao, H. Zhao, L. Yang, and C. Wang, “Intrinsic carrier mobility of germanene is larger than graphene’s: First-principle calculations,” *RSC Advances*, vol. 4, p. 21216, 05 2014.
- [25] Y. Nakamura, T. Zhao, J. Xi, W. Shi, D. Wang, and Z. Shuai, “Intrinsic charge transport in stanene: Roles of bucklings and electron-phonon couplings,” *Electronic Notes in Theoretical Computer Science*, vol. 3, 10 2017.
- [26] G. Le Lay, D. Solonenko, and P. Vogt, *Synthesis of Silicene: Prediction, Synthesis, Application*, 01 2018, pp. 99–113.
- [27] T. P. Kaloni, G. Schreckenbach, M. S. Freund, and U. Schwingenschlgl, “Current developments in silicene and germanene,” *physica status solidi (RRL) Rapid Research Letters*, vol. 10, no. 2, pp. 133–142, 2016. [Online]. Available: <https://onlinelibrary.wiley.com/doi/abs/10.1002/pssr.201510338>
- [28] L. Li, S.-z. Lu, J. Pan, Z. Qin, Y.-q. Wang, Y. Wang, G.-y. Cao, S. Du, and H.-J. Gao, “Buckled germanene formation on pt(111),” *Advanced Materials*, vol. 26, no. 28, pp. 4820–4824, 2014. [Online]. Available: <https://onlinelibrary.wiley.com/doi/abs/10.1002/adma.201400909>
- [29] M. Dávila, L. Xian, S. Cahangirov, A. Rubio, and G. L. Lay, “Germanene: a novel two-dimensional germanium allotrope akin to graphene and silicene,” *New Journal of Physics*, vol. 16, no. 9, p. 095002, sep 2014. [Online]. Available: <https://doi.org/10.1088/1367-2630/16/9/095002>
- [30] M. Derivaz, D. Dentel, R. Stephan, M.-C. Hanf, M. Ahmed, P. Sonnet, and C. Pirri, “Continuous germanene layer on a(111),” *Nano Letters*, vol. 15, p. 25102516, 03 2015.
- [31] M. Dvila and G. Le Lay, “Few layer epitaxial germanene: A novel two-dimensional dirac material,” *Scientific Reports*, vol. 6, p. 20714, 02 2016.
- [32] H. Wang, H. S. Wang, C. Ma, L. Chen, C. Jiang, C. Chen, X. Xie, A.-P. Li, and X. Wang, “Graphene nanoribbons for quantum electronics,” *Nature Reviews Physics*, Sep 2021. [Online]. Available: <http://dx.doi.org/10.1038/s42254-021-00370-x>
- [33] S. Dutta and S. K. Pati, “Novel properties of graphene nanoribbons: a review,” *J. Mater. Chem.*, vol. 20, pp. 8207–8223, 2010. [Online]. Available: <http://dx.doi.org/10.1039/C0JM00261E>
- [34] P. Ruffieux, S. Wang, B. Yang, C. Snchez-Snchez, J. Liu, T. Dienel, L. Talirz, P. Shinde, C. A. Pignedoli, D. Passerone, and et al., “On-surface synthesis of graphene nanoribbons with zigzag edge topology,” *Nature*, vol. 531, no. 7595, p. 489492, Mar 2016. [Online]. Available: <http://dx.doi.org/10.1038/nature17151>
- [35] Y.-W. Son, M. L. Cohen, and S. G. Louie, “Energy gaps in graphene nanoribbons,” *Phys. Rev. Lett.*, vol. 97, p. 216803, Nov 2006. [Online]. Available: <https://link.aps.org/doi/10.1103/PhysRevLett.97.216803>

- [36] O. V. Yazyev and L. Helm, “Defect-induced magnetism in graphene,” *Phys. Rev. B*, vol. 75, p. 125408, Mar 2007. [Online]. Available: <https://link.aps.org/doi/10.1103/PhysRevB.75.125408>
- [37] J. Fernández-Rossier and J. J. Palacios, “Magnetism in graphene nanoislands,” *Phys. Rev. Lett.*, vol. 99, p. 177204, Oct 2007. [Online]. Available: <https://link.aps.org/doi/10.1103/PhysRevLett.99.177204>
- [38] W. L. Wang, O. V. Yazyev, S. Meng, and E. Kaxiras, “Topological frustration in graphene nanoflakes: Magnetic order and spin logic devices,” *Physical Review Letters*, vol. 102, no. 15, Apr 2009. [Online]. Available: <http://dx.doi.org/10.1103/PhysRevLett.102.157201>
- [39] L. Matthes and F. Bechstedt, “Influence of edge and field effects on topological states of germanene nanoribbons from self-consistent calculations,” *Phys. Rev. B*, vol. 90, p. 165431, Oct 2014. [Online]. Available: <https://link.aps.org/doi/10.1103/PhysRevB.90.165431>
- [40] V. Sharma, P. Srivastava, and N. Jaiswal, “Prospects of asymmetrically h-terminated zigzag germanene nanoribbons for spintronic application,” *Applied Surface Science*, vol. 396, pp. 1352–1359, 11 2016.
- [41] M. M. Monshi, S. M. Aghaei, and I. Calizo, “Edge functionalized germanene nanoribbons: impact on electronic and magnetic properties,” *RSC Adv.*, vol. 7, pp. 18 900–18 908, 2017. [Online]. Available: <http://dx.doi.org/10.1039/C6RA25083A>
- [42] A. Karaei Shiraz, A. Yazdanpanah Goharrizi, and S. M. Hamidi, “The electronic and optical properties of armchair germanene nanoribbons,” *Physica E: Low-dimensional Systems and Nanostructures*, vol. 107, pp. 150–153, 2019. [Online]. Available: <https://www.sciencedirect.com/science/article/pii/S1386947718313250>
- [43] (2021, November) The nobel prize in chemistry 1998. Nobel Prize Outreach. nobelprize.org. [Online]. Available: <https://www.nobelprize.org/prizes/chemistry/1998/summary/>
- [44] L. E. F. Foa Torres, S. Roche, and J.-C. Charlier, *Introduction to Graphene-Based Nanomaterials: From Electronic Structure to Quantum Transport*, 2nd ed. Cambridge, MA: Cambridge University Press, 2020.
- [45] J. P. Perdew, K. Burke, and Y. Wang, “Generalized gradient approximation for the exchange-correlation hole of a many-electron system,” *Phys. Rev. B*, vol. 54, pp. 16 533–16 539, Dec 1996. [Online]. Available: <https://link.aps.org/doi/10.1103/PhysRevB.54.16533>
- [46] N. Troullier and J. L. Martins, “Efficient pseudopotentials for plane-wave calculations,” *Phys. Rev. B*, vol. 43, pp. 1993–2006, Jan 1991. [Online]. Available: <https://link.aps.org/doi/10.1103/PhysRevB.43.1993>
- [47] C. Hartwigsen, S. Goedecker, and J. Hutter, “Relativistic separable dual-space gaussian pseudopotentials from h to rn,” *Phys. Rev. B*, vol. 58, pp. 3641–3662, Aug 1998. [Online]. Available: <https://link.aps.org/doi/10.1103/PhysRevB.58.3641>

- [48] P. E. Blöchl, “Projector augmented-wave method,” *Phys. Rev. B*, vol. 50, pp. 17 953–17 979, Dec 1994. [Online]. Available: <https://link.aps.org/doi/10.1103/PhysRevB.50.17953>
- [49] Synopsys. (2021, November) Dft-d and basis-set superposition error. [Online]. Available: https://docs.quantumatk.com/tutorials/dispersion_corrections_and_bsse/dispersion_corrections_and_bsse.html
- [50] C. C. D. Centre. (2021, November) Mercury - crystal structure visualisation, exploration and analysis made easy. [Online]. Available: <https://www.ccdc.cam.ac.uk/Community/csd-community/freemercury/>

Curriculum Vitae

Alexander B. Goldstone received his Bachelor of Science in both Mathematics and Electrical Engineering along with a minor in Japanese from George Mason University in 2016. He graduated Magna Cum Laude with honors in mathematics and Japanese, and is a member of Phi Beta Kappa, Phi Kappa Phi, and the National Japanese Honors Society. Upon graduation he was awarded the 2016 Outstanding Academic Achievement Award from the Volgenau School's Department of Electrical and Computer Engineering and was admitted to the department's PhD program under the Provost Scholarship. As a graduate research assistant he taught both Electromagnetic Theory and the Semiconductor Physics Lab. He received his first position as a civilian researcher at the Federal Night Vision Laboratory at Fort Belvoir in 2019 and later as a contractor through Qinetiq Inc. He currently works at the United States Army Research Laboratory developing II-VI and colloidal quantum dot based IR sensors as a contractor through Sivananthan Laboratories.